# Simultaneous application of two laser-induced fluorescence approaches for film thickness measurements in annular gas-liquid flows

A.V. Cherdantsev[1,2,3], J.S. An[1], A. Charogiannis[1], and C.N. Markides[1,*]

[1] Clean Energy Processes (CEP) Laboratory, Department of Chemical Engineering,
Imperial College London, London SW7 2AZ, UK
[2] Laboratory of Transfer Processes, Department of Multiphase Systems,
Kutateladze Institute of Thermophysics, Novosibirsk 630090, Russia
[3] Laboratory of High Energy Thermal Processes,
Novosibirsk State University, Novosibirsk 630090, Russia

*Corresponding author. Telephone: +44 (0)20 759 41601. Email: c.markides@imperial.ac.uk

**N.B.: This is the PREPRINT (submitted) version of this article.**
**The final, published version of the article, can be found at: [To Appear]**

## Abstract

This paper is devoted to the simultaneous application of two spatiotemporally resolved optical techniques capable of liquid film thickness measurements, namely Planar Laser-Induced Fluorescence (PLIF) and Brightness-Based Laser-Induced Fluorescence (BBLIF), to co-current downward annular gas-liquid flows. A single laser sheet is used to excite the liquid film, which has been seeded with a fluorescent dye, along a longitudinal/vertical plane normal to the pipe wall. Two cameras, one for each technique, are placed at different angles to the plane of the laser sheet in order to recover, independently by the two techniques, the shape of the gas-liquid interface along this section. The effect of the angle between the laser sheet and the PLIF camera axis is also investigated. In film regions where the gas-liquid interface is smooth and flat, the conventional approach used for interpreting PLIF data is affected by total internal reflection of the fluorescent light at the free surface, or "mirror effect", which leads to an overestimation of the film thickness that increases as the angle between the laser sheet and the camera axis is decreased. Nonetheless, local features such as light intensity maxima or minima are often located within the fluorescent signals that correctly identify the true interface, which in these conditions also coincides well with the BBLIF film-thickness measurement. When a correction for the mirror effect based on simple flat-film optical calculations is applied, this leads to PLIF results that correspond well to the true film thickness. Interestingly, it is further found that interfacial three-dimensionality, and in particular azimuthal/circumferential non-uniformity, can lead to underestimation of film thickness by PLIF that in some cases counteracts the overestimation due to the mirror effect. Smaller angles between the laser sheet and camera axis make PLIF less susceptible to this error. In regions where the film surface is rough, including on the surface of disturbance waves, the mirror effect is suppressed. The BBLIF measurement, on the other hand, is affected by loss of signal sensitivity or saturation in thick film regions, as well as distortions at complex or multiple interfaces in agitated flow regions with significant wave activity. Direct comparisons between PLIF and BBLIF measurement data confirm that local overestimations of the film thickness by the latter occur in film regions with higher interfacial curvature, especially at the front slopes of waves and around gas bubbles entrained in the liquid even in smooth films, while underestimations occur in regions with multiple interfaces and inside bubbles although it is often the case that features such as bubbles can be identified and corrected for in simple flows with smooth interfaces. Correction procedures are developed to compensate distortions caused by both methods that make these techniques more accurate for standalone employment. In highly complex, three-dimensional flows, the simultaneous application of both techniques is highly recommended to attain the most reliable information.

**Keywords:** annular flows; liquid films; waves; bubbles; optical measurements; laser-induced fluorescence

# 1. Introduction

## 1.1. Description of annular flows

In annular flows, the liquid phase flows as a thin film along the inner wall of a duct and is in contact with a gas stream which flows through the core of the duct. At sufficiently high liquid and gas flow rates, liquid droplets are entrained in the gaseous core, and gas bubbles are entrained in the liquid film. Annular flows are commonly encountered in industrial equipment such as heat exchangers, evaporators, condensers, absorbers and reactors, and feature in many applications in the chemical and oil and gas industries, as well as in nuclear power plants. The ability to predict the integral characteristics of these flows, such as the mean film thickness, pressure drop, heat transfer and entrained fraction of gas/liquid is vital for the design and operation of relevant industrial facilities. The approach most widely employed for this purpose involves measuring these characteristics directly and creating empirical or semi-empirical correlations between these quantities and important flow parameters. A noteworthy limitation of this approach is that the applicability of such correlations is typically limited to the range of conditions in which they have been developed. This comes as no surprise, as the flow characteristics are affected by numerous factors, including the liquid and gas flow rates, the chemical and physical properties of each phase, the channel geometry, the orientation of flow, the axial distance from the inlet where measurements are collected, the imposed heat flux, and any phase transitions and chemical reactions. A second approach involves building physical models of the flow based on experimental studies of the physical processes of interaction between the phases. This approach is expected to yield more universal results, but is very challenging due to the complexity of the flow phenomena underlying annular flows, even in the relatively simple case of an adiabatic, non-reacting flow.

The film surface in an annular flow is covered by a multiscale system of waves in which disturbance waves dominate. These waves are prominent due to their high amplitude, lifetime, longitudinal size and velocity, and are considered to be the main and necessary source of liquid entrainment (Hewitt and Hall Taylor 1970). They also carry the majority of the liquid flow (Han et al. 2006) and exert a strong influence on the pressure drop (Schubring and Shedd 2011) and heat transfer, including the triggering of nucleate boiling in the case of heated pipe flows (Barbosa et al. 2003). In between disturbance waves, the flow typically comprises a relatively smooth base film, which is several times thinner than the waves.

Another important family of waves that is observed in annular gas-liquid flows is that of small-scale ripples, which are generated at the rear slopes of disturbance waves (Alekseenko et al. 2009). Ripple waves can decelerate and travel across the base film with low speed until the following disturbance wave absorbs them, or accelerate and travel across the top of a disturbance wave until they either decay near the front of the wave, or scatter into ‘liquid bags’ and ‘liquid ligaments’ by the gas stream (Azzopardi 1983; Woodmansee and Hanratty 1969; Pham et al. 2014; Cherdantsev et al. 2014). The generation of fast and slow ripples may be attributed to the vortical motion of liquid below the wave surface (see, for example, the PIV measurements by Zadrazil and Markides 2014, who recently confirmed the presence of recirculation zones in disturbance waves). The disruption of fast-moving ripples is the main mechanism of liquid entrainment in annular flows; the entrained droplets eventually deposit back onto the film either as ‘craters’, with possible entrainment of secondary droplets, or ‘furrows’, with possible entrapment of gas bubbles into the liquid film, depending on the angle of impingement (Cherdantsev et al. 2017).

## 1.2. Overview of experimental methods in annular flows

The experimental investigation of the wavy structure of annular flows presents significant challenges, and imposes rigorous requirements on the experimental technique, such as the ones listed below:

1) High temporal resolution (i.e., high sampling frequency) due to the high velocity of the large-scale disturbance waves and fast ripples, which are typically of the order of several m/s.

2) High spatial resolution in order to resolve the small-scale ripple waves, which have a typical wavelength of the order of a few mm.

3) High measurement dynamic range as the film thickness may vary from about several tens of μm, up to a few mm for the same flow condition.

4) Experiments should be resolved in space and time simultaneously, due to the coexistence and interaction of waves of different types, length scales and time scales.

5) The physical size of the interrogation region and the recording duration should be large enough in order to study these interactions.

6) Ideally, the measurements should be resolved along both the longitudinal and azimuthal/circumferential flow coordinates, as most wave phenomena (e.g., disturbance and ripple waves) are three-dimensional.

7) The measurement technique should be non-intrusive and allow, if possible, for the simultaneous measurement of other flow quantities, such as the velocity field, species concentration and the temperature across the liquid domain.

The above requirements become even more pressing if the processes of entrainment and deposition of droplets and entrapment of gas bubbles are of interest, since the interfacial that relate to these processes are associated with even smaller scales, higher velocities, more complex spatiotemporal behaviour and an even stronger degree of three-dimensionality. In addition, the challenges associated with space- and time-resolved measurements in annular flows, which include the restricted fluid domains under observation and the intermittent nature of the wavy and moving interface, are exacerbated by the emergence of interface regions with steep slopes and high curvature, as well as the generation of a large number of bubbles inside the film or liquid entrainment, which may cause significant measurement errors.

A wide range of experimental techniques have been developed, or adapted from different research fields for the investigation of the interface topology of liquid films in gas-liquid annular flows. Direct high-speed imaging, for example, is useful when studying the dynamics of disturbance waves, as well as various flow processes such as gas/liquid entrainment and deposition, as it can be employed with high spatial and temporal resolution; however, it generally does not provide quantitative information on the film thickness, except when an appropriately calibrated camera is placed at right angles to a longitudinal section of the flow at the outer surface (Pham et al. 2014) or inside the pipe (Hewitt et al. 1990; Pan et al. 2015; Setyawan et al. 2016).

Conductance probes are amongst the most widely employed instrumentation in annular flow studies. They are manufactured in two main electrode configurations, namely ‘flush-mounted probes’ (Chu and Dukler 1974; Webb and Hewitt 1975; Azzopardi 1986; Zhao et al. 2013) and ‘parallel-wire probes’ (Karapantsios et al. 1989; Han et al. 2006). The main limitation of the former is their low spatial resolution, which results in an underestimation of the amplitudes of waves with wavelengths comparable to the probe size. Probe miniaturization can only partially address this issue, as the maximum measureable film thickness falls with the probe size. In a number of papers, complex systems of multiple flush-mounted conductance probes were presented and employed to perform spatiotemporally-resolved film thickness measurements (Sekoguchiet al. 1985; Damsohn and Prasser 2009; Belt et al. 2010). These studies have enhanced our understanding of the evolution of interfacial waves in annular flows, but the limited spatial resolution on offer remains an unresolved issue. Twin-wire probes usually offer better resolution along with a linear sensitivity dependence on film thickness, so that the distance between the wires can be reduced in order to improve the spatial resolution. Nonetheless, such probes disturb the flow, and can affect any measurements conducted further downstream. Thus, the use of multiple sequentially-mounted probes should be avoided when possible. It should also be

noted that the probe itself is affected if a capillary meniscus is formed between the wires, which is highly likely when a high concentration of bubbles is present in the liquid film (van der Meulen 2012).

Optical measurement techniques, and specifically laser-based techniques, are excellent alternatives to the aforementioned measurement methods, as they are non-intrusive (as long as any chemical or particle additives do not affect the main fluid properties or flow characteristics) and also because their spatial and temporal resolution can often be adjusted to meet the requirements of a particular application. The laser-focus displacement (LFD) method (Hazuku et al. 2008), for example, offers good spatial resolution, even though it can only be used to conduct point measurements and is compromised in flows where the interface slope exceeds 33 °, as well as in the presence of bubbles. Similarly, a method based on total internal reflection (TIR) proposed by Hurlburt and Newell (1996) also only offers the ability to conduct point measurements, and is limited by the presence of large interface gradients (in this case, the slope of the interface cannot exceed 5 ° if accurate measurements are required).

In the context of experimental annular flow investigations, two optical methods based on the principle of laser-induced fluorescence (LIF) have been used for film thickness measurements, which differ mainly in the way the fluorescence emission is collected, and by extension, in the way the collected data are treated. In both cases, the liquid is seeded with a dye that emits fluorescent light in a different spectral range than the excitation/laser wavelength; the fluorescence is collected by a camera, which is typically equipped with an optical filter. The first approach is known as planar laser-induced fluorescence (PLIF) and employs a laser sheet to illuminate a section of the flow. The emitted fluorescence can be used to image the film cross-section along the axial direction of the flow directly, and thus to measure its spatial extent in the radial direction of the flow, while also detecting bubbles inside the liquid film and droplets in the gas phase, allowing for the study of such phenomena simultaneously with the wave dynamics. This approach was employed in the annular flow investigations of Schubring et al. (2010), Farias et al. (2012) and Zadrazil et al. (2014). It can achieve high spatial and temporal resolutions simultaneously, and the collected data are expected to be insensitive to the presence of interfacial curvature, bubbles and droplets. Another advantage of PLIF is that it can be used simultaneously with particle image or tracking velocimetry (PIV/PTV) in the same measurement plane in order to recover velocity field information from within the liquid film, as was done, for example, by Zadrazil and Markides (2014) and Charogiannis et al. (2015). A limitation of the standard implementation of this technique, owing to its inherently two-dimensional (2-D) nature, is in performing 3-D measurements, which are possible, for example, with laser-sheet scanning, but challenging. Information in the third dimension (circumferentially) can be obtained by measuring transverse film-thickness profiles, as was done by Farias et al. (2012). A second limitation is related to the so-called ‘mirror effect’ caused by TIR of the fluorescent light at the liquid-gas interface (film free surface), as examined analytically via ray tracing by Häber et al. (2015); this effect is of direct interest to the present study.

The second commonly employed LIF approach is known as brightness-based LIF or BBLIF. In this case, the camera is located near the laser so that the angle between the excitation and imaging planes is reduced as much as possible. The fluorescence intensity (image brightness) at each location along the interrogation region is recorded by the camera (which is again equipped with an optical filter), and is converted to a local film-thickness measurement according to the Beer-Lambert law. This method was used in point-wise configuration by Hewitt et al. (1964) and by Lel et al. (2005), while field measurements of planar falling films, including 3-D measurements, were performed by Liu et al. (1993), Adomeit and Renz (2000), Vlachogiannis and Bontozoglou (2001), Alekseenko et al. (2005), Alekseenko et al. (2015a), Kharlamov et al. (2015). BBLIF was also used specifically to study the structure of liquid films in annular flows with both 2-D (Alekseenko et al. 2009; 2014; 2015b) and 3-D (Alekseenko et al. 2012; Cherdantsev et al. 2014) configurations, together with droplet entrainment and deposition, and bubble entrapment (Cherdantsev et al. 2017). BBLIF can be more easily resolved in two spatial coordinates simultaneously in order to reconstruct the 3-D shape of the interface.

BBLIF can also detect droplets above the interface and bubbles inside the liquid film, allowing detailed investigations of the complex interactions between droplets, bubbles and waves. A noteworthy shortcoming of BBLIF measurements arises when the interface is curved, which introduces a measurement error that increases gradually with wave steepness and is significant when the angle of TIR, which is approximately 48 ° for an air-water interface, is approached. Bubbles are still detectable and measureable with this technique, but the thickness of the film encompassing the bubble can only be approximated. In contrast to PLIF, BBLIF does not offer direct imaging across the excitation plane and thus, cannot be combined readily with PIV/PTV.

There are numerous other methods that are based on a similar measurement principle to BBLIF, such as the light absorption (Clark et al. 2001), pigment luminance (Ohba and Nagae 1993) and near-infrared attenuation (Dupont et al. 2016) technique; however, to the best of our knowledge, these are not widely employed. In addition, there are more complex methods employing different physical principles, such as X-ray tomography (Fisher and Hampel 2010), NMR tomography (Bonn et al. 2008), gamma densitometry (Sharaf et al. 2011), cold neutron tomography (Takenaka et al. 1998) and ultrasonic methods (Chen et al. 2005). The application of the majority of the aforementioned techniques involves significant purchasing costs, and is subject to limitations including limited spatial or temporal resolution, low measurement accuracy in thin-film regions, significant safety hazards, and the inability to resolve the measurements in more than one dimension.

### 1.3. Problem statement and overview of the paper

In the present work, the wavy structure of liquid films in gas-liquid annular flows is investigated by simultaneous application of PLIF and BBLIF. This combination allows us to perform, for the first time, a close evaluation and direct comparison of the two techniques in terms of their ability to recover some of the characteristic features of annular flows, including the measurement of disturbance waves and bubbles. To this end, a series of experiments were conducted in downward annular flows in a vertical pipe (inner diameter 32.4 mm), at a distance of approximately 100 pipe diameters downstream from the flow inlet. According to Webb and Hewitt (1975), two wave-regimes dominate downward annular flows, namely the dual-wave regime and the regular disturbance-wave regime. In the experiments described in this present paper we investigate both flow regimes, and discuss the ability of PLIF and BBLIF to resolve the distinct film topologies that ensue.

In Section 2, we provide a description of the experimental apparatus and the measurement techniques that we employ, and in Section 3, we present qualitative as well as quantitative analyses of the different error sources and optical distortions relevant to our two selected LIF techniques, i.e., PLIF and BBLIF. Furthermore, we examine the effect of the angle between the PLIF camera and the laser sheet by conducting experiments using the conventional 90 ° arrangement, as well as a 70 ° arrangement. Finally, Section 4 is devoted to direct quantitative comparisons of film thickness statistics (first and second moments, probability densities) that were obtained by the two techniques, and to the proposal of correction procedures aimed at moderating the errors associated with each of the techniques in standalone implementation.

## 2. Experimental methods

### 2.1. Experimental apparatus and conditions

PLIF and BBLIF measurements were conducted in downward annular flows in a vertical pipe with an inner diameter $D = 32.4 \pm 0.4$ mm and a total length $L = 5$ m. The main vertical pipe was made of Fluorinated Ethylene Propylene (FEP) in order to match the refractive index of water ($n_{FEP} = 1.334$ and $n_{water} = 1.334$ at 532 nm at 25 ° C). The liquid phase was tap water seeded with Rhodamine 6G dye at a concentration of 8 mg/L. A schematic of the experimental apparatus is provided in Fig. 1. The liquid was circulated through the closed flow-loop using a variable-speed, vertical multi-stage centrifugal pump (CRIE 3-15, Grundfos;

labelled "JO1" in Fig. 1), and was introduced into the test section via a conical injector that generated circumferentially uniform liquid films (for more details, see Zhao et al. 2013). At the measurement location, which is at the farthest end of the pipe from the inlet, the pipe was partially enclosed in a Perspex box with 80-mm sides and a length of 1.3 m, and the free volume between the pipe and the box was filled with water to minimize any optical distortions caused by the curved pipe wall. After flowing out of the vertical-pipe test section, the gas and liquid phases were separated in the receiving tank, labelled "F01" in Fig. 1.

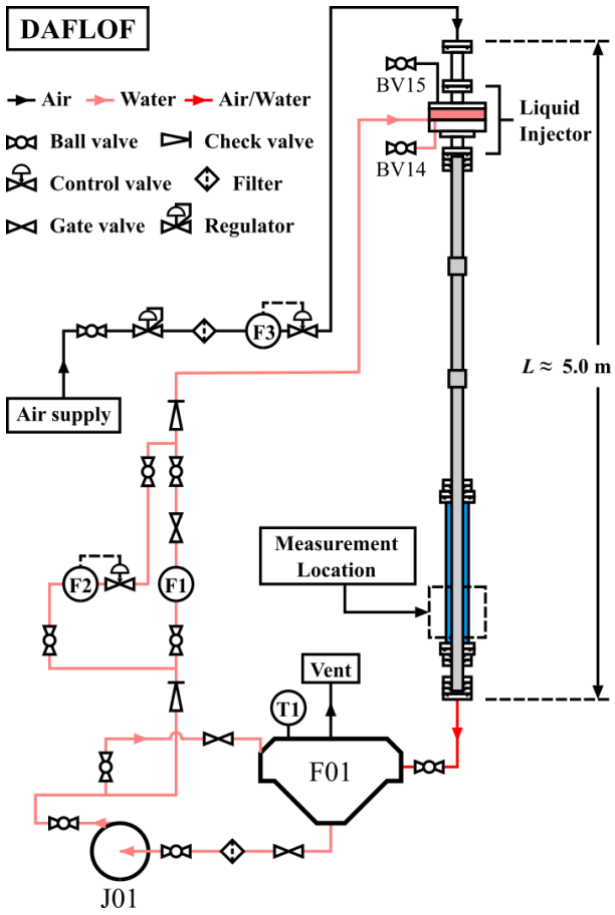



**Figure 1**: Flow facility schematic showing the inlet section, FEP pipe, correction box at the measurement location, as well as the flow loop comprising the tank, pump and mass-flow controllers and air supply.

Experiments were performed over the range of liquid and gas flow rates summarized in Tables 1 and 2. At high flow rates ($\geq 2-3$ L/min), the liquid flow rate $Q_L$ was controlled by a turbine flow-meter (F110-X LCD, Fluidwell, labelled "F1" in Fig. 1) with an accuracy of ± 0.5 %, while at low flow rates ($\leq 2-3$ L/min) it was measured by a Coriolis mass-flow controller (M15, Bronkhorst, "F2") with an accuracy of ± 0.2 %. The gas flow rate $Q_G$ was measured by a thermal mass-flow controller (M+W Instruments, Bronkhorst, "F3") with a manufacturer stated accuracy of ± 0.2 %. The superficial gas velocity, defined as $V_G = 4Q_G/\pi D^2$, which in annular (thin-film) flows is approximately equal to the bulk gas-phase velocity, was varied from zero to a maximum of ~ 40 m/s in steps of ~ 4 m/s, covering a range of corresponding gas-phase Reynolds numbers, $Re_G$, from 0 to 85,100. The liquid-phase Reynolds number, $Re_L$, was varied from 140 to 1,330. Here, the Reynolds numbers of the gas and liquid phases are defined as $Re_G = 4Q_G/\pi D\nu_G$ and $Re_L = Q_L/\pi D\nu_L$, where, $\nu_G$ and $\nu_L$ are the kinematic viscosities of air and water. The liquid phase may be also characterised by the bulk liquid velocity, $V_L = Q_L/\pi D\langle h\rangle$, where $\langle h\rangle$ is the mean film thickness. Based on a measure of $\langle h\rangle$ that was taken to be an average between the two LIF measurements, the bulk liquid velocity spanned the range from 0.02 to 0.17 m/s. Therefore,

the investigated flows spanned a range of kinematic velocity ratios $V_G/V_L$ from 0 to ~ 63 (at the highest $Re_G$ and lowest $Re_L$). The experimental matrix consisted of 66 points (11 gas flow rates and 6 liquid flow rates).

**Table 1.** Experimental matrix of the investigated liquid flow rates.

| $Q_L$ [L/min] | $V_L$ [m/s] | $Re_L$ [-] |
|---|---|---|
| 0.8 | 0.02 | 140 |
| 1.7 | 0.03 | 300 |
| 3.2 | 0.07 | 500 |
| 5.1 | 0.10 | 800 |
| 6.6 | 0.14 | 1,040 |
| 8.4 | 0.17 | 1,330 |

**Table 2.** Experimental matrix of the investigated gas flow rates.

| $Q_G$ [L/min] | $V_G$ [m/s] | $Re_G$ [-] |
|---|---|---|
| 0 | 0.0 | 0 |
| 200 | 4.1 | 8,700 |
| 400 | 8.1 | 17,500 |
| 600 | 12.1 | 26,200 |
| 800 | 16.2 | 34,900 |
| 1,000 | 20.2 | 43,700 |
| 1,200 | 24.3 | 52,400 |
| 1,400 | 28.3 | 61,100 |
| 1,600 | 32.4 | 69,900 |
| 1,800 | 36.4 | 78,600 |
| 1,950 | 39.4 | 85,100 |

At high gas-flow velocities, some variation of the liquid flow rate was observed, which was of the order of 5 % of the flow rate at zero gas-velocity (see Fig. 7 for a flow regime map representative of our experiments). The temperature of the working fluid was monitored throughout the duration of the experimental runs using a K-type thermocouple, which was installed in the collection tank. At medium and high gas-velocities the liquid temperature was approximately 18 °C, while at the low gas-velocities the temperature was a few degrees higher, possibly due to heating imparted to the liquid flow by the pump and the flow meter. This was especially noticeable when the Coriolis flow meter was used, which resulted in heating of the liquid flow to 25 – 27 °C. All the measurements were performed at a distance of 100 $D$ downstream of the liquid injector.

### 2.2. Experimental procedure

A pulsed Nd: YAG laser (Nano-L-50-100PV, Litron Lasers, $\lambda$ = 532 nm, pulse energy 50 mJ, 10 ns pulse duration, 100 Hz pulse-rate) was used for the excitation of the dye-doped liquid phase. The laser beam was converted to a thin vertical sheet (the width of the sheet was approximately 0.5 mm) using a dedicated sheet generator, and was focused at the inner pipe-wall. The sheet optics, and therefore the laser sheet, was

inclined downwards at an angle of about 15 ° from the vertical in order to limit the occurrence of reflections at selected locations along the waves while accepting intensified reflections elsewhere. Two 8-bit CMOS cameras (VC-Imager Pro HS 500, LaVision), each with 1,024 × 1,280 pixels, were employed for recording the fluorescence emitted from the liquid phase in the region of interrogation (ROI), one for each technique, and were aimed at approximately the same flow region. Both cameras were equipped with Sigma 105 mm f/2.8 macro lenses and 540 nm long-pass filters. The BBLIF camera was positioned next to the sheet optics with its axis at an angle of 15 ° relative to the excitation plane, while the PLIF camera was positioned with its axis at an angle of either 90 ° or 70 ° relative to the excitation plane (see Fig. 2). The PLIF camera angle was varied in order to investigate its effect on the PLIF film-thickness measurement. This resulted in two separate sets of experiments, referred to as PLIF90 and PLIF70, respectively. The BBLIF camera and the sheet optics were placed at the same position in both measurement sets.

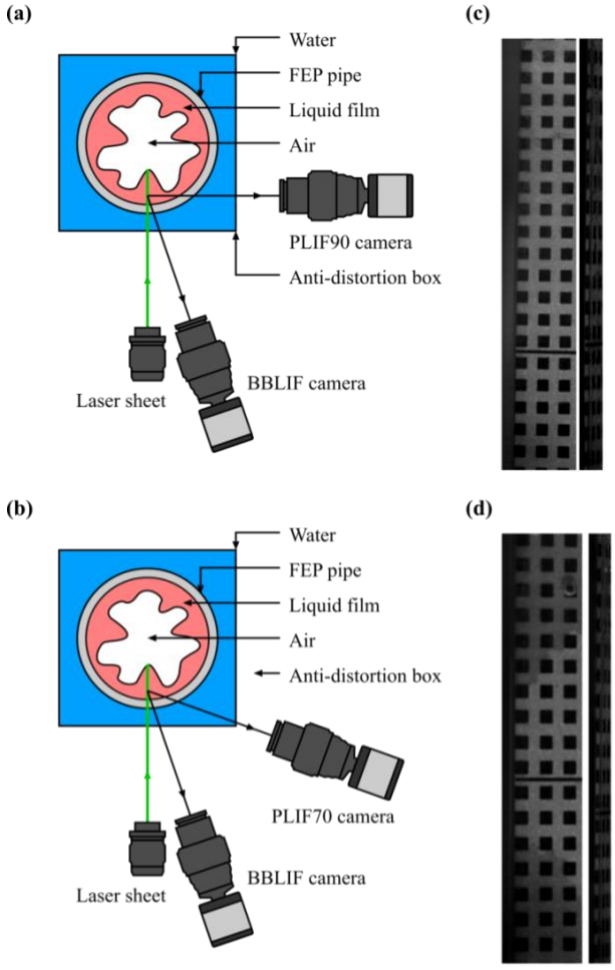



**Figure 2**: Experimental arrangement for: (a) simultaneous PLIF90 and BBLIF, and (b) simultaneous PLIF70 and BBLIF, along with corresponding images of a spatial correction/calibration graticule immersed in the flooded pipe obtained by using the PLIF (in left of frame) and BBLIF (in right of frame) cameras for each of the two configurations: (c) PLIF90 and BBLIF, and (d) PLIF70 and BBLIF.

In order to recover the spatial resolution of the two cameras in the axial and radial directions of the flow, and also to ensure that the same flow region was imaged by the camera pair, a calibration graticule was inserted in the pipe. The graticule was aligned with the excitation plane and the pipe was flooded with the working liquid. Images of the graticule taken by the PLIF90 and PLIF70 cameras are shown on the left-hand side (of the vertical white line) in Fig. 2(c) and 2(d), respectively, while the graticule image collected by the

BBLIF camera is shown on the right-hand side of both subfigures. The dimensions of each black square correspond to 1 mm × 1 mm, and the pitch to 2 mm. The pipe wall is located to the left these frames. The horizontal line within the square pattern was used to identify the relative location of the imaging window of each camera. Despite the fact that the fields of view (FOV) of the PLIF and BBLIF cameras did not overlap completely, the overlap region extended over a sufficiently large portion (~ 90 %) of the resulting images. The transform used to relate the FOV of each camera was obtained by linear approximation of the coordinates (in pixels) of several squares in the calibration-graticule images. The physical extent of the overlapping region was 34.3 mm in the PLIF90 and 31.5 mm in the PLIF70 configurations. The spatial (pixel) resolution of the PLIF90 camera was 30.6 μm/pixel in both the axial and the radial directions, while in the case of the PLIF70 camera, the resolution was 26.6 μm/pixel in the axial direction and 28 μm/pixel in the radial direction of the flow. The spatial resolution of the BBLIF camera was 26.7 μm per pixel.

The frame rate of the laser used in this work was limited to 100 Hz. This frame rate is not sufficient for conducting a fully temporally-resolved study of the examined flows, nevertheless, the instantaneous shape of the interface was resolved and recovered simultaneously by the two cameras, which sufficed in meeting the objectives of our present work. For each pair of flow rates (i.e., liquid and gas), a continuous record of 1,000 frames was generated, corresponding to a recording duration of 10 s.

Examples of raw PLIF70 and BBLIF frames are presented in Fig. 3(a) for a flow with $Re_L$ = 500 and no gas shear. When the film surface is smooth, as in these frames, ghost images can also be clearly discerned in each camera frame. The origin of these artefacts is illustrated in Fig. 3(b). The ghost line marked on the BBLIF frame is attributed to the emission of fluorescence by the liquid-film on the opposite wall, while ghost line marked on the PLIF frame originates from a reflection of the fluorescence emitted by the ROI, about the interface at the left-hand-side and opposite to the PLIF camera. The main reason for opting for the 15 ° offset angle in the case of BBLIF was to avoid overlapping the two signals (i.e., the emission from the excited region of the flow and that from the opposite side of the pipe). It is also interesting to note that both ghost images are highly curved due to the waviness of the interface on the opposite side of the pipe. We will show later on that in the disturbance-wave regime, where the interface is significantly more agitated than in these images, the ghost images dissipate over larger areas and nearly disappear.

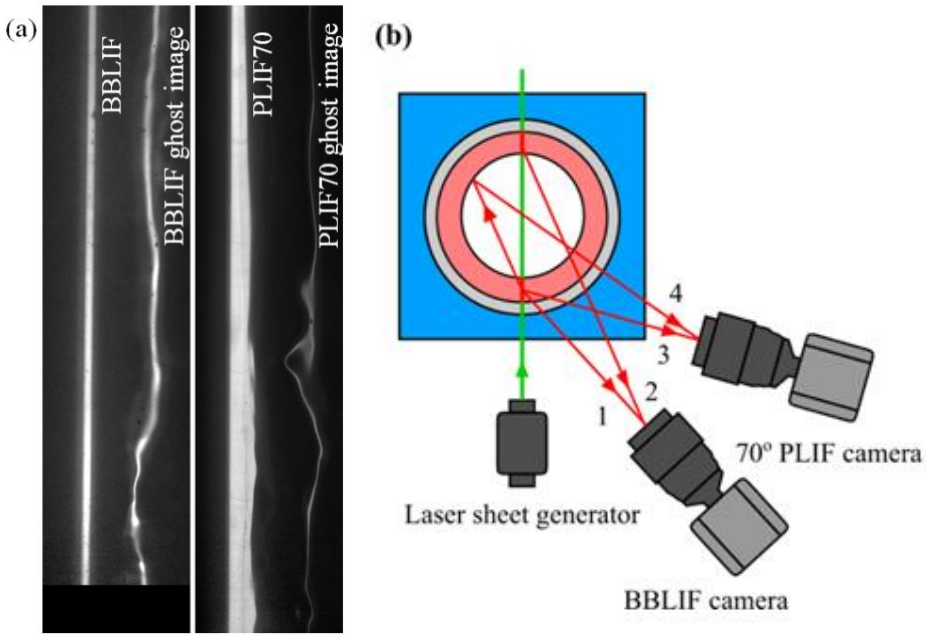



**Figure 3**: (a) Example raw BBLIF image and PLIF70 image from a flow with $Re_L$ = 520 and $Re_G$ = 0, showing the fluorescence signal collected by the BBLIF camera originating from the ROI, the fluorescence

signal collected by the BBLIF camera originating from the film opposite to the ROI, the fluorescence signal collected by the PLIF70 camera originating from the ROI, and a reflection of this fluorescence from the gas-liquid interface at the wall opposite to the PLIF camera. (b) Schematic showing the optical paths that relate to the appearance of the fluorescence emission and reflections thereof in the PLIF and BBLIF images.

### 2.3. Brightness-based laser-induced fluorescence (BBLIF)

In the case of BBLIF, the first data-processing step is to identify the centreline of the illuminated area of the flow (e.g., the leftmost bright line in Fig. 3(a)) and to form a spatiotemporal matrix of raw brightness from the entire frame record generated in each flow condition. In a second step, each value of local and instantaneous brightness is then converted into a film-thickness measurement by integrating the Beer-Lambert law, which in accordance with the procedure described in Alekseenko et al. (2014) leads to the equation:

$$J(x) = C(x)\left(1 - \mathrm{e}^{-\alpha h(x)}\right)\left(1 + K\mathrm{e}^{-\alpha h(x)}\right) + D(x), \quad (1)$$

where $J(x)$ is the brightness of the fluorescence registered by a single camera-pixel, $C(x)$ is a compensation matrix, $\alpha$ is the absorption coefficient of the employed fluorescent dye, $K$ is the reflection coefficient at the air-water interface, $D(x)$ is the dark level of the camera and $h(x)$ is the local film thickness at axial position $x$. It is possible, instead of the single-pixel intensity value at the centreline of the illuminated area, to use the averaged intensity over a certain spanwise/circumferential region in the BBLIF images, which will act to improve the single-to-noise ratio, but also to give rise to a loss of resolution in that direction. The choice is available depending on the details of the application of the technique and the desirable outcomes from the measurement.

Beyond the primary fluorescence emission in response to the original excitation light, Eq. (1) also accounts for the fraction of the excitation light that is reflected at the gas-liquid interface (free surface) back towards the wall, thereby re-exciting the dye in the liquid and leading to an additional (secondary) fluorescence emission, and this is done by assuming that the original and reflected light rays are collinear and fully overlap. In actual flow measurements this will not be the case, and any off-axis reflections will result in re-excitation of a different volume of fluid. In the limit that no reflected light crosses the original optical path this leads to an underestimation of local film thickness of up to 2 % (= $K$; see below), which is negligible. However, a more substantial overestimation may result elsewhere in the film due to the local re-excitation caused by the off-axis reflections, which depending on the interface angle can be as low as a few % but as high as 40 – 50 % where the interface slope is steep. This is discussed in more detail in Section 3.3.

The reflection coefficient, $K$, in Eq. (1) is set to a constant value of 0.02, while $\alpha$ depends on the dye concentration (here, Rhodamine), so its value is usually determined experimentally by measuring the brightness of the fluorescence emission in two slots of known thickness that are filled with Rhodamine-seeded water. The obtained brightness values are then inserted into Eq. (1), together with the path lengths, yielding a system of two equations, which were transformed into a single equation for $\alpha$, and solved numerically. For the Rhodamine concentration employed in this work of 8 mg/L, $\alpha$ = 0.25 mm$^{-1}$, with an error associated with this measurement of $\alpha$ estimated at ~ 10 %. The contribution of this error to the film-thickness measurement error is illustrated in Fig. 4(a), where normalized $J(h)/J(h_o)$ values are plotted as a function of $h$ for values of $\alpha$ ± 5 % (dashed) and ± 10 % (solid) from the used value of $\alpha$ = 0.25 mm$^{-1}$. When brightness is recalculated into film thickness, from Eq. (1), the deviation due to the uncertainty in the value of $\alpha$ results in a film-thickness measurement error, which, as shown in Fig. 4b, increases for thicker films. For large waves with thicknesses above $h$ = 3 mm, which are of particular interest in these flows, the film-thickness deviation can be ≈ 6 %; the largest waves identified by PLIF in the present work had $h$ > 6 mm, at which thickness the deviation is ≈ 18 %. Furthermore, it should be noted in relation to Fig. 4 that as expected from any such absorption method, the measurement sensitivity decreases at progressively thicker films and

ultimately leads to signal saturation. This requires attention at the experimental design stage in selecting the appropriate sensitivity and dynamic range of the measurement depending on what is of interest.

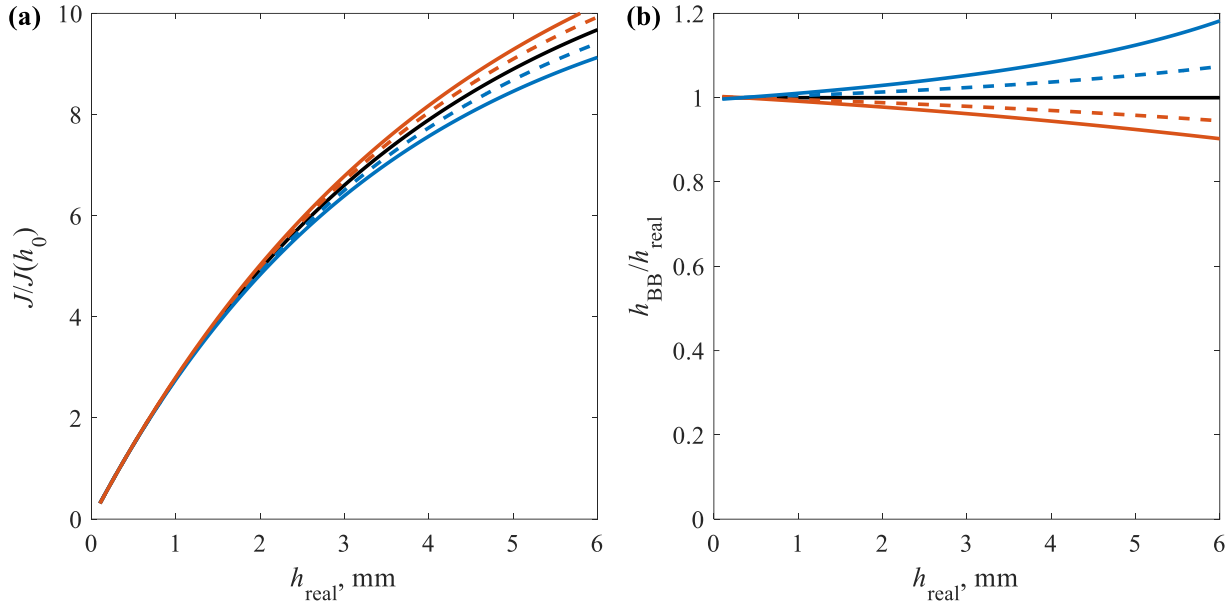



**Figure 4**: (a) Normalized (by the reference film-thickness) brightness, as a function of the film height $h_{real}$ for different values of the absorption coefficient $\alpha$. (b) Corresponding ratio of film thickness measured by BBLIF with erroneous $\alpha$ to the real film thickness. In both plots, $\alpha$ = 0.25 mm$^{-1}$ (black), ± 5 % (dashed) and 10 % (solid).

The compensation matrix $C(x)$ is used to relate the measured brightness on the imaging frame to the corresponding local film thickness, and also to compensate for the non-uniform energy distribution along the laser sheet, and the spatially non-uniform response of the camera sensor. In order to obtain $C(x)$, an *in situ* reference signal is required, such as the time-averaged brightness, $\langle J_0(x)\rangle$, emitted by a liquid layer of known thickness $h_0$, from which $C(x)$ can be obtained from:

$$C(x) = \frac{\langle J_0(x)\rangle - D(x)}{(1 - e^{-\alpha h_0})(1 + Ke^{-\alpha h_0})} \quad (2)$$

Previously (e.g., in Alekseenko et al. 2013, Alekseenko et al. 2014), this reference signal was obtained by setting up a falling-film flow with zero gas velocity and low $Re_L$ (i.e., $Re_L \approx$ 20 – 40). The main advantage of this method is that $h_0$ can be approximated as being equal to the Nusselt film thickness (Nusselt, 1916) since the film waviness is suppressed and the interface is relatively flat with little three-dimensionality. Here, it was impossible to obtain such a flow as FEP (i.e., the pipe material) is highly hydrophobic and falling liquid films broke into rivulets for $Re_L$ < 100. The thinnest continuous film flow that could be obtained without dewetting was for $Re_L$ = 40 at the highest $Re_G$ = 85,100; a condition that could be used for calibration based on the average film-thickness reported by Alekseenko et al. (2013), $h_0 \approx$ 0.12 mm. A second option was to use the average film-thickness from a falling-film flow with $Re_L$ = 140 (and $Re_G$ = 0), assuming that the Nusselt formula still provides a reasonable prediction of $h_0$ (in this case, $h_0 \approx$ 0.33 mm). It should be noted that although the liquid temperature increased for these conditions as we noted earlier (i.e., $T$ = 27 °C in this case), the emission of Rhodamine 6G is nearly insensitive to temperature variations, and thus, a reference signal obtained at a different temperature can be used without introducing significant bias error. Both methods were used to recover film-thickness data from annular flows, but the second method was selected for further processing, as the weaker reference signal that was obtained using the first method was more susceptive to camera noise.

Particular attention must also be paid to the correction associated with the dark level of the camera, $D(x)$, which increases over time. For this reason, the collection of dark-level measurements throughout the duration of the experiments is advised. Overall, the systematic error arising from the aforementioned dependencies of $J(x)$ in the absence of optical distortions related to any interfacial slopes is estimated at ≈ 5 %. Random errors also arise due a multitude of factors, including the camera noise, the pulse-to-pulse variation of the laser power, and any drift in the laser power. The total random error for the present BBLIF experiments is estimated at 10 %. One of the reasons for this is the low dynamic range of the camera, which corresponds to 8 bits. Using a 12-bit camera, instead, helps reduce this error (see the estimates given in Alekseenko et al. 2014).

Finally, the maximum film thickness measurable by BBLIF is subject to limitations stemming from the geometrical configuration of the excitation and collection optics. In more detail, the transverse cross-section of the illuminated liquid volume can be approximated as a rectangle with height equal to the instantaneous local film thickness, $h$, and width equal to the sheet thickness, $W$. In our experiments, the thickness of the laser sheet was set to a relatively low value ($W \approx 0.5$ mm) in order to improve the spatial resolution of the measurements in the tangential direction of the flow. Given a viewing angle of 15 ° for the BBLIF camera, the maximum film thickness that can be measured using this particular configuration is equal to $W/\tan(15°)$, which corresponds to approximately 2 mm. Any further increase in the film thickness will not contribute to the collected brightness, whose intensity will appear to saturate, resulting in an underestimation of the film thickness. This error can be suppressed by employment of a thicker laser sheet, at the expense of increased spatial averaging along the circumferential direction of the flow, or a 3-D BBLIF-configuration as used by Alekseenko et al. (2012) and Cherdantsev et al. (2014). However, the reflection errors at the complex 3-D interface and their influence on the total emission that were discussed above will also be exacerbated in this case.

### 2.4 Planar laser-induced fluorescence (PLIF)

PLIF film-thickness measurements are based on the identification of the two liquid boundaries, the solid-liquid interface, which coincides with the pipe wall, and the gas-liquid interface. In this study, the location of the solid-liquid interface was obtained from calibration-graticule images such as the ones shown in Fig. 2(c) and 2(d). In generating these images, a graticule was inserted into the pipe and aligned with the excitation plane, the pipe was flooded with the working liquid, and the location of the pipe wall was then assumed to coincide with the end of the printed regular-square pattern on the graticule. As an alternative to this approach, the solid-liquid interface can be identified from the intensity profiles in PLIF images obtained either with the pipe flooded, or directly during the experimental runs. This approach was employed, for example, by Charogiannis et al. (2015) and Charogiannis et al. (2017) in their study of the hydrodynamic characteristics of planar falling films by simultaneous application of PLIF and PTV, in order to ensure that any misalignment between the graticule and the excitation plane, or between the square pattern and the component it is attached to (i.e., substrate or channel wall) does not induce a systematic error in the location of the solid-liquid boundary. In the present experiments, the identification of the solid-liquid interface by employment of this approach was not robust, with images from different flow regimes resulting in different wall positions despite the use of the same identification criteria. Therefore, the first approach was selected. It is noted that an incorrect identification of the wall location can result in a corresponding systematic error in the measurement of film thickness, which is higher for thin films; for example, a 1 – 2 pixel offset in the current optical arrangement correspond to ≈ 25 – 50 μm, or a ≈ 5 – 10 % relative error locally in a film with a thickness of ≈ 500 μm. This can be overcome by zooming into the film and increasing the spatial resolution of the measurement, however, this sacrifices the extent of the captured ROI in the flow direction.

The location of the gas-liquid interface in previous studies was identified by using a fluorescence-intensity threshold (Schubring et al. 2010; Farias et al. 2012; Zadrazil et al. 2014; Kokomoor and Schubring 2014), or based on the local gradient of the fluorescence intensity profile (Charogiannis et al. 2015; Markides

et al. 2016; Charogiannis et al. 2017). The second method may be less suitable for highly-agitated films due to the presence of multiple false interfaces, and therefore, a threshold approach was preferred in this study with the signal gradient only used as an auxiliary criterion. The selection of an appropriate threshold is challenging, as the excitation energy (and, thus, intensity on the resulting frames) varies along the imaged domain, as well as over time due to the pulse-to-pulse variation of the laser power and any long-term energy drift. In addition, Schubring et al. (2010) reported that thicker film regions glow brighter compared to thinner regions, likely due to the enlarged illuminated liquid volume in the azimuthal direction caused by scattering of the laser light by the optical section, and also the brightness of the emitted fluorescence will be affected locally by the presence of bubbles or steep slopes at the interface, the pipe wall and the film interface. The combination of these factors suggests that a reliable threshold selection method should involve locally and instantaneously (pixel-by-pixel and frame-by-frame) adjusted threshold values that can account for the specific characteristics of the flows under observation, however, this was not attempted in the present work as it was decided to investigate the effectiveness of PLIF in the absence of such processing complexity.

In previous studies, different methods were employed to address the aforementioned challenges. Zadrazil et al. (2014), employed auxiliary manual identification of the interface in order to adjust the intensity threshold along the excitation plane as suggested above, while Schubring et al. (2010) and Farias et al. (2012) 'stretched' the brightness distribution of the obtained images at every $x$ between the maximum and minimum levels. In the present work, the threshold intensity for each combination of $t$ and $x$ (i.e., for every image and location along the image, or image column) was set to the arithmetic average of the maximum and minimum brightness in that column of image $J(x,y)$. The raw PLIF images (see, e.g., Fig. 5(a)) were then binarized using this threshold and closed morphologically to dampen the effect of random noise. The edges in the binarized images (Fig. 5(b)) were marked and concatenated into lines consisting of dots connected to each other.

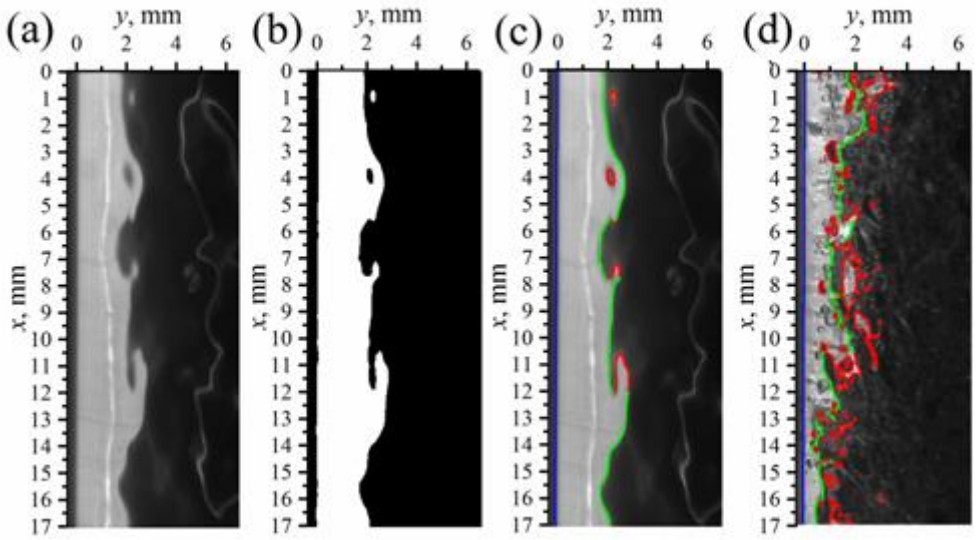



**Figure 5**: Examples of gas-liquid interface identification using PLIF data: (a) Raw PLIF70 image from a flow with $Re_L$= 520, $Re_G$ = 0, (b) binarized version of (a), (c) processed version of (a), (d) processed PLIF70 image from a flow with $Re_L$ = 1,330, $Re_G$ = 43,700. The red lines show the edges of the binarized and morphologically closed PLIF interfaces, and the green lines the final selected interface locations.

Another challenge associated with the processing of PLIF image relates to the observation of out-of-plane features. Schubring et al. (2010) and Zadrazil et al. (2014) suggested that some of these features maybe associated with droplet entrainment, however, they may also stem from ghost images (see Fig. 3(a)) or from fluorescent light emitted by film regions outside the excitation plane. To identify such artefacts in the PLIF

images and discard them from the film-thickness measurements, Schubring et al. (2010) employed a smooth-interface criterion, alongside manual identification and removal of outliers (Kokomoor and Schubring 2014).

In the present work, the border lines corresponding to the gas-liquid interface in each binarized image were identified using a processing algorithm in which, firstly, for each column along the binarized image, the signs of the local brightness-gradients, $J(y+1)-J(y-1)$, were obtained. Border lines were then identified at the $y$-coordinates where the sign changed. The objective of this step was to obtain a linear array of interface coordinates, $Y(x)$. The lines were then sorted according to the sum of the signs of the gradients along their length. At this stage, the discarding process was initialized, starting with the longest lines with the most stable negative sign; if an image-column (i.e., one $x$-coordinate along the PLIF frame) had more than one $y$-coordinate assigned to it, the lowest $y$-coordinate (i.e., the one closer to the wall) was selected as the gas-liquid interface location for that value of $x$. If for a sub-range of $x$ values belonging to a border line, $Y(x)$ was already obtained during the previous steps, the new $y(x)$ were compared to those already assigned to the interface location, and the larger values were discarded. This process allowed us to eliminate most out-of-plane features. If the whole range of $x$ belonging to a line was already written in $Y(x)$, the new line was discarded completely. This step allowed us to remove any lines corresponding to the borders around bubbles entrapped in the liquid film. The processing routine was terminated when the sum of the signs of a line reached a positive value.

In order to assess the validity of our algorithm, auxiliary images were created with the identified liquid boundaries superimposed over raw PLIF frames. Examples of such images are presented in Fig. 5 for different flow conditions, with the red lines marking the interfaces found using the edge-detection technique described above, and the green lines showing the final $Y(x)$ values. Based on visual inspection of a large number of images spanning a wide range of flow conditions and film topologies, good agreement was observed between the identified interfaces and the visible borders of the illuminated regions of the flow. In smooth films (see, e.g., Fig. 5(c)), the algorithm is effective in removing any structures resembling ‘overturning waves’, which are non-physical in these flows. In rougher films (see, for example, Fig. 5(d)), the algorithm discards most out-of-plane features, and most of the time, any bubbles entrained within the liquid film.

Larger uncertainties, mainly in the PLIF90 measurement, were observed when the film thickness was very small (typically below 150 – 200 μm), as the signal from the film occupied smaller regions of the resulting images, and the brightness across the image was reduced locally to levels closer to the background signal level. For PLIF70, this occurred rarely and primarily when a bubble occupied almost the entire film thickness (i.e., when it extended between the wall and the free surface); for PLIF90, in contrast, this occurred more frequently and even in films that did not contain bubbles, resulting in the appearance of ‘dry spots’ which were not observed with PLIF70. To address this issue during the processing of the PLIF90 images, a threshold was used when low PLIF90 to BBLIF film-thickness ratios were observed. When the peak brightness fell below this adjusted threshold, the corresponding PLIF90 data were not processed further, and the film thickness was set to 150 μm. In standalone PLIF applications this limitation can be overcome by employing a higher dye concentration or laser intensity, and/or a thicker laser sheet, while it would also be necessary to consider zooming closer to the film and increasing the spatial resolution of the measurement.

## 3. Qualitative observations and comparisons

### 3.1. Flow regimes

A regime map of downward annular flows was first presented by Webb and Hewitt (1975), who identified four main wave patterns in these flows: ripples, dual waves, thick ripples and regular disturbance waves. The transition from the dual-wave to the disturbance-wave regime is the most pertinent and the most prominent across the range of flow conditions we have examined in the present work. Webb and Hewitt (1975) identified this transition from the shape of the temporal spectra they generated from film thickness records,

while Alekseenko et al. (2015b) used spatiotemporal film-thickness data instead. In the present set of experiments, a distinction between regular disturbance-waves and the other flow regimes is made based on qualitative observations of the film surface using both PLIF and BBLIF images (i.e., similar to Zadrazil et al. 2014), as well as by tracking the film roughness over the examined range of liquid and gas flow rates. A particular consequence of strong agitation, which signifies the transition from the dual-wave to the disturbance-wave regime, is the entrapment of bubbles in the liquid film, which is most prominent for the largest waves. This is demonstrated in Fig. 6, where raw PLIF70 and BBLIF images are presented for flows with $Re_L$= 300 for $Re_G$ = 34,900, 43,700 and 52,400. In each subfigure, the frame on the left corresponds to a raw BBLIF image, while that on the right shows a raw PLIF70 image.

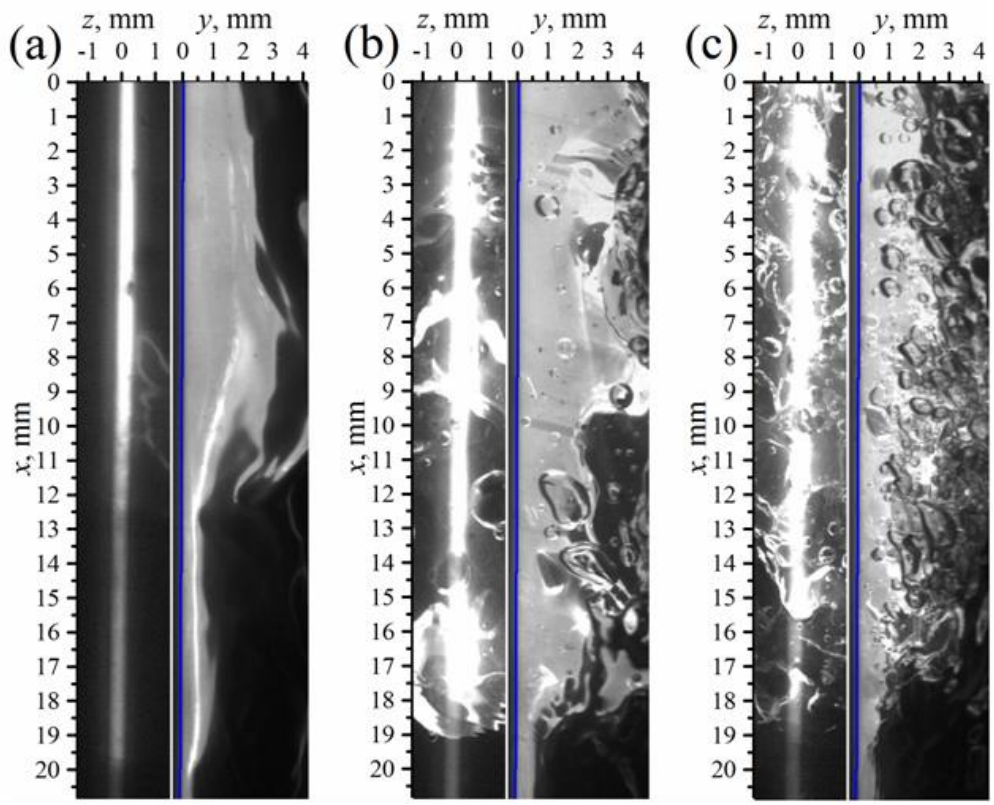



**Figure 6**: Raw PLIF70 and BBLIF images of waves in flows with $Re_L$ = 300 and: (a) $Re_G$ = 34,900, (b) $Re_G$ = 43,700 and (c) $Re_G$ = 52,400. In each subfigure, the frame on the left shows a raw BBLIF image, and the frame on the right shows a raw PLIF70 image. The blue lines indicate the wall location.

The regime map obtained from the present experiments is superimposed over that proposed by Webb and Hewitt (1975) in Fig. 7. In general, two major types of interfacial wave behaviours are identified over the range of investigated flow conditions in the present experiments, signified by either filled or empty circles in Fig. 7. The filled circles represent flow regimes that feature the appearance of disturbance waves, i.e., large and fast-moving waves with highly agitated surfaces, strong interfacial complexity, and the frequent entrapment of bubbles in the liquid films and entrainment of liquid in the gas flow. The empty circles represent regimes where large waves also appear, but are relatively smoother with a smaller degree of dimensionality. One further intermediary regime is also observed. In the points marked by crosses in Fig. 7 the mean film thickness is higher and the film thickness distributions are narrower and nearly symmetrical around the average. This observation fits the description of the 'thick-ripple' regime introduced by Webb and Hewitt (1975) and also discussed by Zadrazil et al. (2014). Finally, a few transitional flow cases are marked by half-filled circles. The two maps are in qualitative agreement, however, the transition from dual-wave to regular disturbance-wave

regime appears in our case to be slightly shifted towards lower liquid and gas flow rates. This discrepancy may be attributed to the different criteria used to identify the transition, and also to the smaller pipe diameter used in our experiments (32.4 mm compared to 38.2-mm ID). The second argument is further supported by the findings of Alekseenko et al. (2015b), who observed the same transition at even lower flow rates in a 15-mm ID pipe.

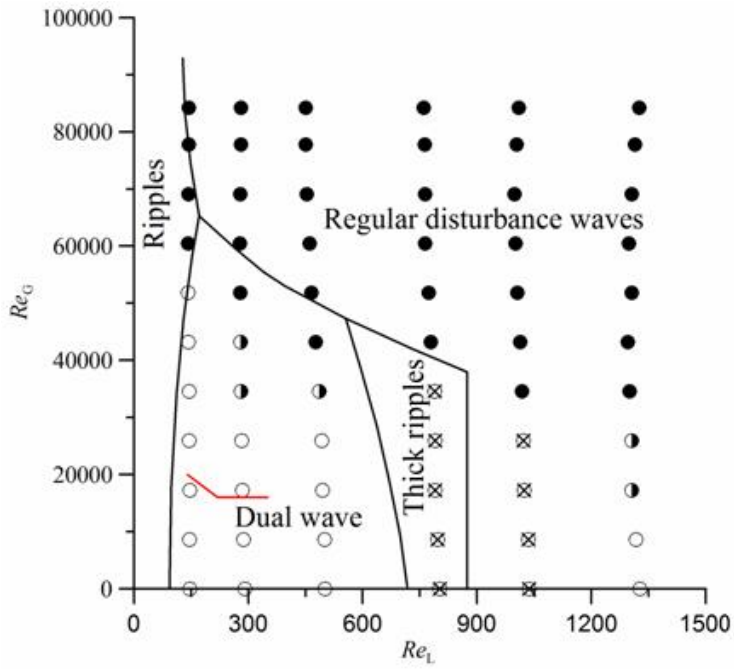



**Figure 7**: Downward annular flow wave-regime map. The black lines indicate the wave-pattern transitions proposed by Webb and Hewitt (1975) based on their measurements in a 38.2-mm pipe, and the red line indicates the transition reported by Alekseenko et al. (2015b) in a 15-mm pipe.

### 3.2. Smooth films

In Fig. 8, we present comparisons between local and instantaneous PLIF90, PLIF70 and BBLIF film-thickness measurements from a falling film with $Re_L$ = 140 and no gas shear. Close inspection of these frames reveals that, generally, in these flows which are characterised mainly by smooth and relatively flat films, the instantaneous film-thickness profiles obtained by BBLIF lie lower than those obtained by PLIF. This discrepancy between the PLIF and BBLIF measurements appears more pronounced for PLIF70 than PLIF90. In contrast, a case of the front of a wave is shown in Fig. 8(a) where the film appears thicker in the BBLIF measurement than in the corresponding PLIF90 measurement.

A prominent feature that can be observed in both PLIF frames is a distinct bright line (in some cases dark line) inside the fluorescing region of the flow, which was also apparent in some of the earlier PLIF data presented by Zadrazil et al. (2014). Interestingly, the location of this line coincides with the location of the gas-liquid interface that is recovered by BBLIF, which suggests that this intensity feature does indeed mark the true gas-liquid interface location. Further evidence in support of this view is the observation (on occasion) of bubble reflections about such bright lines, as well as the interruption of thin darker lines visible in the raw PLIF images when they cross these lines. Such darker lines are most likely shadows cast by tiny non-uniformities of the pipe wall or inside the optical box. The observation of a fluorescing liquid-volume above the bright lines is most likely related to the mirror effect due to TIR that was described theoretically by Häber et al. (2015). According to their model, the fluorescence emitted by the illuminated region of the flow travels in all directions, with part of it collected directly by the camera creating the real image of the film,

and part of it undergoing TIR at the gas-liquid interface between the excitation plane and the camera, thus creating a false (second) image of the film above the true image.

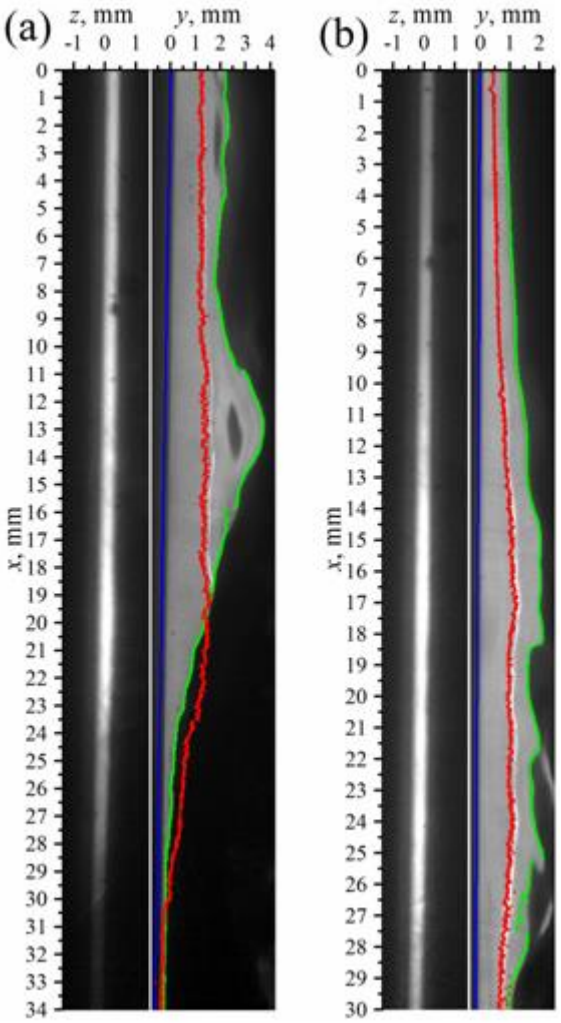



**Figure 8**: Gas-liquid interfaces identified by PLIF and BBLIF in smooth and flat film regions in a flow with $Re_L$ = 300 and $Re_G$ = 0: (a) PLIF90, and (b) PLIF70. In each subfigure, the frame on the left shows a raw BBLIF image, and the frame on the right shows a raw PLIF image with superimposed gas-liquid interfaces recovered from PLIF (green) and BBLIF (red). The blue lines indicate the wall location.

A pronounced difference between our experimental observations and the predictions of Häber et al. (2015) relates to the shape of the PLIF intensity profiles through the liquid film in the wall-normal direction, *y*. Example profiles from our PLIF measurements are shown in Fig. 9, which demonstrate that instead of the 'ramp profile' predicted in Häber et al. (2015), we in some cases observe a local intensity peak or trough, possibly owing to the circumferential slope of the interface, even when no distinct feature is observed inside the liquid film in the images. As mentioned above, the location of this peak or trough in these smooth and flat film regions agrees with the location of the gas-liquid interface obtained from BBLIF, which indicates that this identifies correctly the true gas-liquid interface, as do other features such as bubble reflections and the interruption of shadows from the wall. Even in the present measurements, the local intensity peak/trough, along with the aforementioned features such as bubble reflections, etc., can be used to generate accurate statistics of the film thickness from selected locations and instances where they are observed, however, this is not pursued further in order to focus on conventional applications of the PLIF technique.

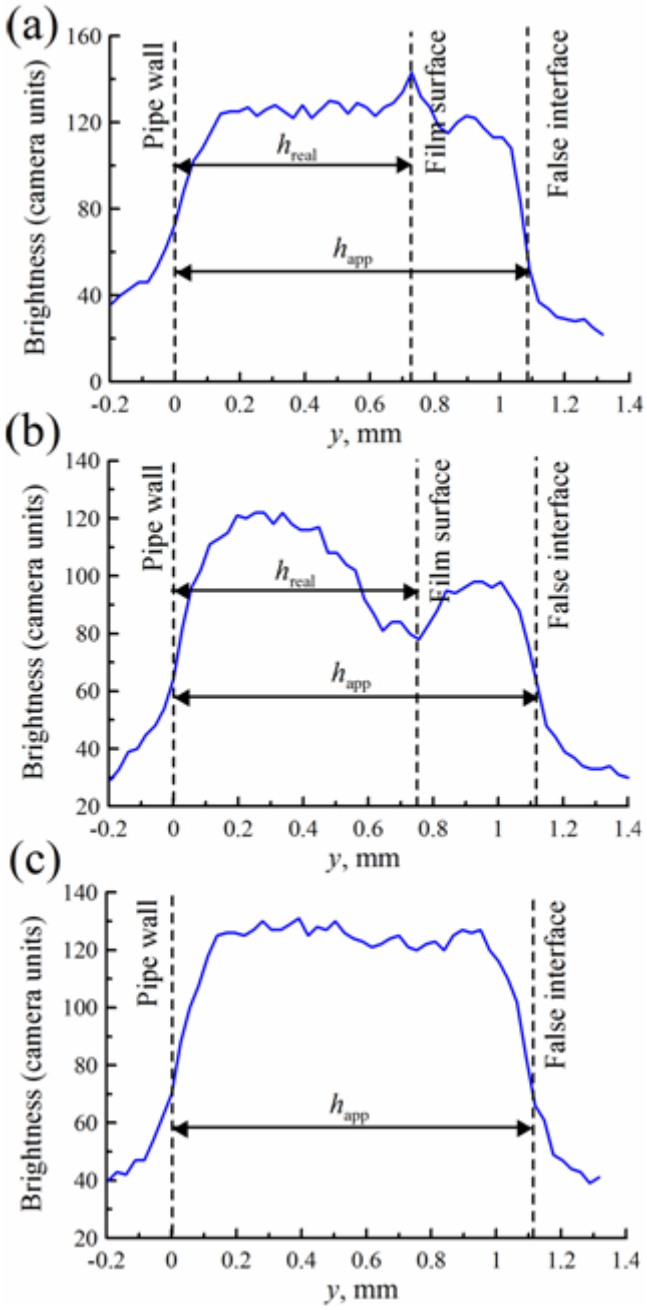



**Figure 9**: Examples of wall-normal fluorescence-intensity profiles recovered from smooth-film regions in PLIF70 images, showing the location of the apparent gas-liquid interface. The true interface is observed as: (a) a peak in the profile, or (b) as a trough in the profile, or (c) cannot be observed at all.

It is expected that in the case of raw PLIF70 images, the false interface will be found further away from the true interface, which suggests that the true extent of the film will be overestimated more than in the case of PLIF90 if left uncorrected. In order to investigate the effect of the observation angle on raw PLIF images, we performed ray-tracing calculations for non-wavy films (i.e., similar to those performed by Häber et al., 2015). The geometry of our model system is presented in Fig. 10(a) for PLIF90 and Fig. 10(b) for PLIF70. The ray forming the upper border of the false film image is emitted at Point A, which is adjacent to the wall, and is reflected at the interface at Point B, along the camera axis and at right angles to the imaging plane. Furthermore, Line *c* represents the perpendicular distance from Point B to Line OA, which corresponds to the wall normal at the measurement/illumination plane, and *d* the distance from the interface to the end of

Line *c*, which in PLIF90 also coincides with the thickness of the false image of the film, and effectively corresponds to the overestimation of the true film-thickness, *h*.

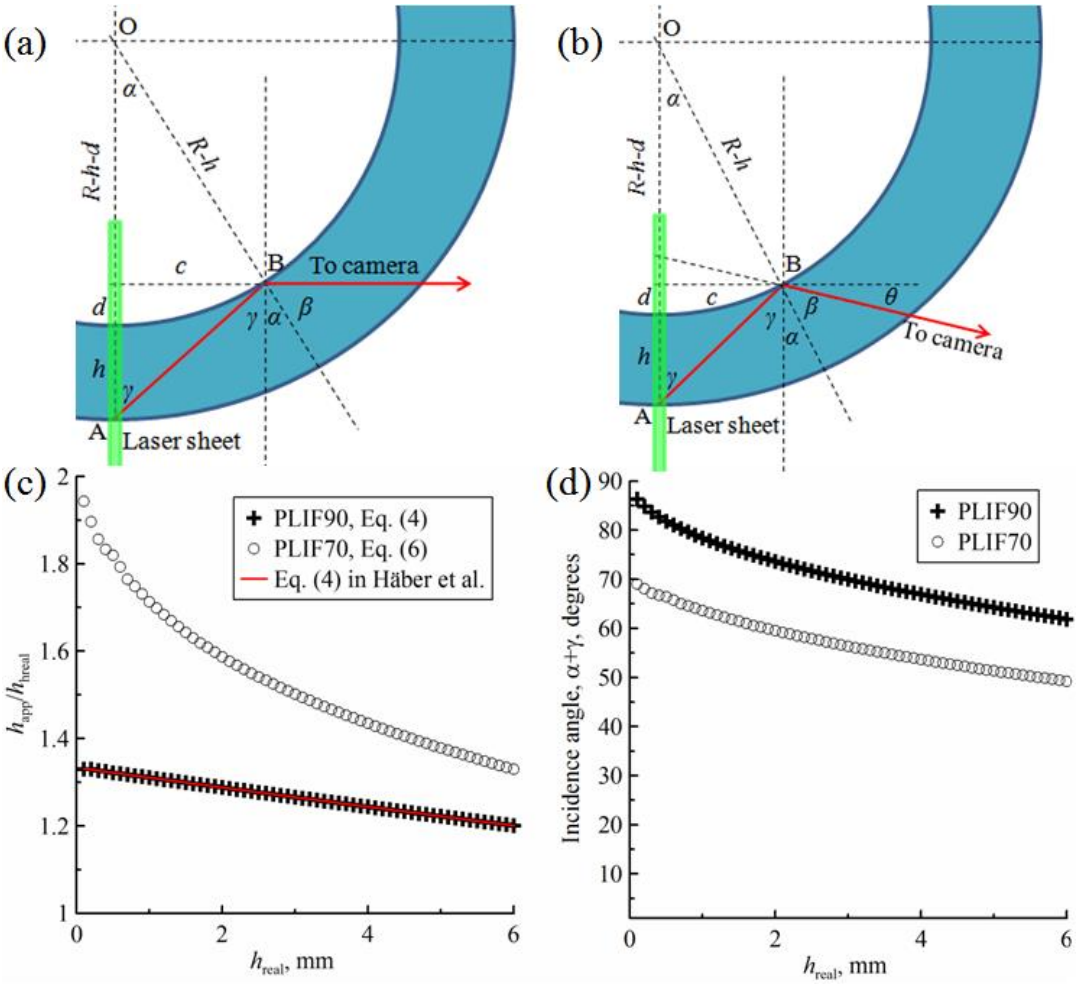



**Figure 10**: Estimation of the location of the false interface recovered by ray-tracing for: (a) PLIF90, and (b) PLIF70 ($\theta$ = 20 °). (c) Overestimation of the film thickness by PLIF as a function of the film thickness for PLIF70 and PLIF90, based on $2R = D$ = 32.4 mm. (d) Interface incidence angle, $\alpha+\gamma$, for PLIF90 and PLIF70 as a function of the true film thickness.

For PLIF90, the spatial extent of the total film image, $h + d$, is obtained from the system of equations:

$$\beta = \alpha + \gamma;\ \ \beta + \alpha = \frac{\pi}{2};\ \ c = \sqrt{d(2(R-h)-d)};\ \tan(\alpha) = \frac{c}{R-h-d};\ \tan(\gamma) = \frac{c}{h+d} \qquad (3)$$

where $R$ is the inner radius of the pipe, $h$ is the true thickness of the uniform film, $d$ is the thickness of the false film image, $\alpha$ is the angle AOB and $\gamma$ is the angle OAB, as shown in Fig. 10(a). The interfacial angle of incidence is equal to $\alpha + \gamma$, which is also equal to the angle of reflection, $\beta$. This system can be reduced into a single equation which is solved numerically to obtain $d$ at a given $h$ (and for a known $R$):

$$\tan^{-1}\left(\frac{\sqrt{d(2(R-h)-d)}}{R-h-d}\right) = \frac{\pi}{4} - \frac{1}{2}\tan^{-1}\left(\frac{\sqrt{d(2(R-h)-d)}}{h+d}\right) \qquad (4)$$

The overestimation of the true film-thickness can then be expressed as the ratio of the apparent to the true film-thickness, $h_{app}/h_{real}$, which corresponds to $(h+d)/h$ and is plotted in Fig. 10(c) as a function of $h$, which matches the analytical approximation by Häber et al. (2015) shown as a continuous red line.

When PLIF is instead implemented with the angle between the camera axis and the excitation plane being < 90 °, i.e., $\theta$ > 0 °, the ratio $h_{app}/h_{real}$ is equal to $(h + d + \sqrt{d(2(R-h)-d)}\tan(\theta))/h$. The geometry of this system is described in Fig. 10(b), and Eq. (3) is rewritten as:

$$\beta = \alpha + \gamma;\ \beta + \alpha + \theta = \frac{\pi}{2};\ c = \sqrt{d(2(R-h)-d)};\ \tan(\alpha) = \frac{c}{R-h-d};\ \tan(\gamma) = \frac{c}{h+d} \qquad (5)$$

and Eq. (4) becomes:

$$\tan^{-1}\left(\frac{\sqrt{d(2(R-h)-d)}}{R-h-d}\right) = \frac{\pi}{4} - \frac{1}{2}\tan^{-1}\left(\frac{\sqrt{d(2(R-h)-d)}}{h+d}\right) - \frac{\theta}{2} \qquad (6)$$

In the case of $\theta$ = 20 ° in Fig. 10(c), it can be seen that the overestimation of the film thickness by PLIF70 is indeed greater than that of PLIF90, as expected. Very thin films, e.g., with $h$ < 0.5 mm, are overestimated by > 80 %, whereas thick films, e.g., with $h$ > 4 mm, are overestimated by < 40 %.

In Fig. 10(d), we also plot the interface incidence angle, $\alpha$+$\gamma$, as a function of the film thickness from the same set of equations. For both PLIF70 and PLIF90, this angle is always greater than the angle of TIR for the range of examined film thicknesses. Nevertheless, our calculations show that this angle decreases with increasing $\theta$ and eventually becomes lower than the TIR angle; if $\theta \geq 45$ ° is used, the incidence angle will be lower than this critical value for nearly the entire film-thickness range of interest to us thereby avoiding the appearance of the false interface, although at the cost of a reduced spatial resolution. The planar falling-film investigations of Charogiannis et al. (2015; 2017) employed $\theta \approx 52 - 56$ °, which resulted in the appearance of a false image of the film, however, the brightness of the false image was much weaker than that of a real image making their distinction relatively straightforward. This is of interest, as it suggests that the false interface need not be avoided altogether, and that it may be enough to increase $\theta$ up to a point (beyond the 20 ° tested in the present work in PLIF70) where the emission intensity of the false film image is clearly discernible from that of the true film and warrants further investigation.

### 3.3 Interface gradients and total internal reflection

The local brightness of the emitted fluorescence in BBLIF is directly proportional to the total (integrated) excitation energy, which has a contribution from both the (primary) incident laser light transmitted from the wall into the fluid, and from the (secondary) light reflected at the interface back towards the wall, as mentioned earlier in Section 2.3. BBLIF is known to be sensitive to reflections, the extreme case of which is TIR of the excitation light at steeper interface slopes. TIR in our flows is expected to occur when the angle between the transmitted light and the normal to the interface overcomes 48.5 °, however, the reflection contribution increases gradually from smaller angles, which impacts the BBLIF measurement.

In more detail, we consider here how the actual value of the reflection coefficient, $K$, can differ from the assumed constant value used in Eq. (1), for the simple case of collinear light paths. In general, $K$ depends on the refractive indices of air ($n_a$ = 1) and water ($n_w$ = 1.334), the angle $\theta_i$ between the incident laser light and the normal to the interface, which is related to the interface slope (N.B.: here, we assume that the angle does not change the light path), and the angle of refraction $\theta_t$. This dependence is described by the Fresnel equations, and for un-polarized light (in this case, the fluorescence emission) is given by:

$$K = \frac{1}{2}\left[\left(\frac{n_w\cos\theta_i - n_a\cos\theta_t}{n_w\cos\theta_i + n_a\cos\theta_t}\right)^2 + \left(\frac{n_w\cos\theta_t - n_a\cos\theta_i}{n_w\cos\theta_t + n_a\cos\theta_i}\right)^2\right],\quad \cos\theta_t = \sqrt{1 - \left(\frac{n_w}{n_a}\sin\theta_i\right)^2} \qquad (7)$$

Since the interface slope is unknown, $K$ in Eq. (1) is set to a constant value of 0.02, which corresponds to a flat film with $\theta_i$ = 0. When the slope of the interface is shallow, the real reflection coefficient, $K$, is in

fact approximately equal to 0.02, which is also the value imposed on this parameter, and the measurement error will be mainly determined by the camera noise, the non-uniform sensitivity of the sensor and the pulse-to-pulse variation of the laser, and is estimated at up to 10 % in the present BBLIF experiments. In this case, the contribution from any reflected light is small, and also taken into account explicitly in Eq. (1), which is expected to make BBLIF a reliable technique for the measurement of smooth and (near-)flat films. However, when the slope is steep, the contributions from reflected light are larger and not accounted for.

In Fig. 11(a), we plot $K$ as a function of $\theta_i$ and observe that, indeed, when the film is flat, $K \approx 0.02$ over a wide range of $\theta_i$. On the other hand, the actual value of $K$ experienced in a flow starts to increase appreciably relative to this constant value as the interface slope increases to values in excess of $\theta_i$ = 30 – 35 ° and approaching $\theta_i$ = 48.5 °, which corresponds to the angle of TIR, resulting in progressively larger measurement errors. Specifically, $K$ attains values of 0.025 at $\theta_i$ = 30 °, 0.06 at 40 °, 0.15 at 45 ° and 0.50 at 48 °. Fig. 11(b) shows an estimation of the effect exerted on the BBLIF measurements by the additional illumination due to increased $K$, which is not taken into account by Eq. (1). Specifically, average film thickness overestimates of around 5 % at $\theta_i$ = 40 °, 10 – 15 % at $\theta_i$ = 45 ° and 40 – 50 % at $\theta_i$ = 48 ° are expected, which also depend on the local film thickness. Beyond 48.5 °, the light undergoes TIR and the contribution of the reflected/secondary emission becomes comparable to, or even exceeds if the reflected light is focused locally by the curved interface, the primary emission from the transmitted light. Due to the nonlinear relation between the emitted brightness and the film thickness, this may result in considerable overestimations of the film-thickness.

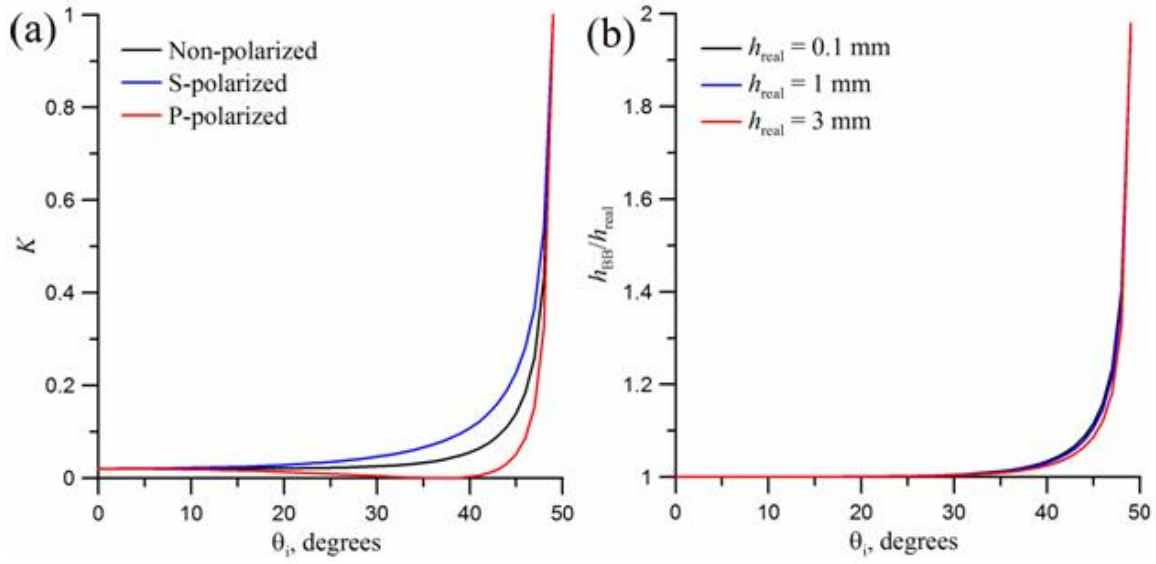



**Figure 11**: (a) Reflection coefficient at the air-water interface $K$, plotted as a function of the incidence angle $\theta_i$ of the excitation light. (b) Estimation of the effect of $K$ on the BBLIF measurement.

On this basis, in flow regions where the slope of the interface is small, we expect BBLIF to be a reliable technique for film-thickness measurements, whereas in rough wave regions with large interfacial slopes or multiple interfaces, either at the free-surface or internally due to entrainment of gas inside the liquid film, which are expected when measuring complex or agitated interfacial film flows, BBLIF is expected to yield errors in the film-thickness measurements due to this effect. The observation of interface gradients that trigger significant measurement errors is rare in smooth and flat films, e.g., falling films at low $Re_L$, as well as along the base film in rougher film-regimes, which is typically populated by relatively low-amplitude, slow-moving ripples. With increasing liquid and gas flow rates, however, the probability of encountering waves with steeper slopes increases, as does the occurrence of TIR. Examples of such waves are shown in

the BBLIF images of Fig. 12, which show bright streaks stretching along the tangential direction of the flow appearing at the sloping regions between the crests and troughs of 3-D, high-amplitude waves. These intensity peaks render the direct identification of the true interface impossible.

We should also note in Fig. 12 that in the proximity of these steep film regions, the location of the interface identified by PLIF70 often appears close to the bright line observed directly in the raw PLIF images, in contrast with the prediction of Eq. (9). Thus, in smooth flows with occasional large waves, $h_{BB}$ is lower than $h_P$ when the interface slope is low (as discussed in the previous section), and $h_{BB}$ exceeds $h_P$ substantially when the interface slope is high. In between those two regions, the two coincide near the edges of the peaks in the BBLIF measurements that signal the onset of steeper interface-slopes. In smooth films, any regions where the TIR angle is exceeded (in the BBLIF measurements) can be identified based on the high local gradients in $h_{BB}(x)$, and often be accounted for. When, however, the interface is agitated, for example at higher $Re_G$ and $Re_L$, as well as in the presence of bubbles, the observation of steep slopes is commonplace and the identification of film regions that are plagued by TIR becomes very challenging.

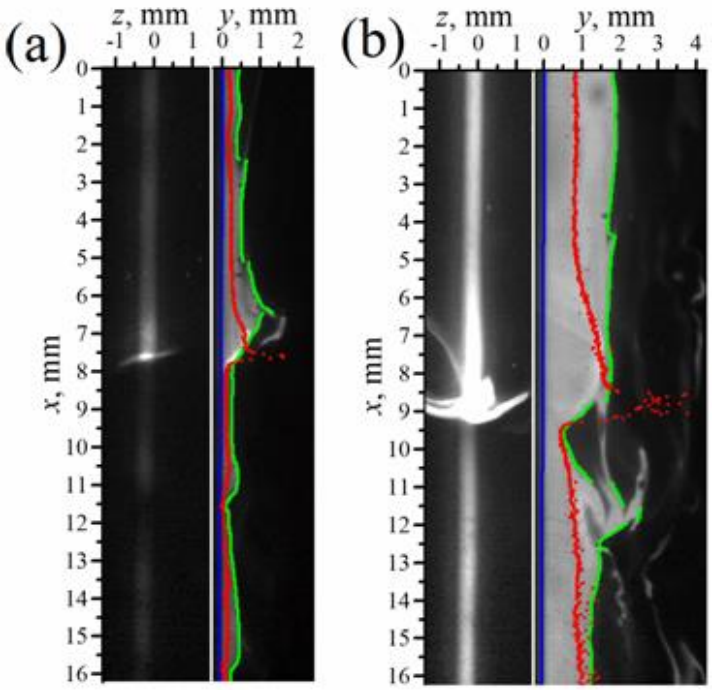



**Figure 12**: Erroneous BBLIF measurements at wave fronts in flows with: (a) $Re_L$ = 140 and $Re_G$ = 69,900, and (b) $Re_L$ = 300, $Re_G$ = 43,700. The coloured lines are explained in Fig. 8.

We now proceed to discuss the effect of the transverse curvature of the film on the two measurement methods. Earlier we mentioned that PLIF (especially PLIF90) sometimes shows lower film-thickness values compared to BBLIF in smooth and flat films where the latter can be considered reliable. We hypothesise here that this observation may be linked to the longitudinal but also transverse slopes of the interface, and by extension to the three-dimensionality of the wavy films. Waves with significant 3-D features and negative transverse curvature are often encountered in falling films (see, for example, Kharlamov et al., 2015, who described horseshoe and streak waves), while the ripples in gas-sheared films, as well as the disturbance waves themselves, are also highly three-dimensional (see, for example, Cherdantsev et al., 2014). This curvature is expected to affect both measurement techniques but in different ways as illustrated in Fig. 13, which shows an interface encountered between the PLIF90 camera and excitation plane, and an interface at the BBLIF measurement location that is at an angle to the excitation plane.

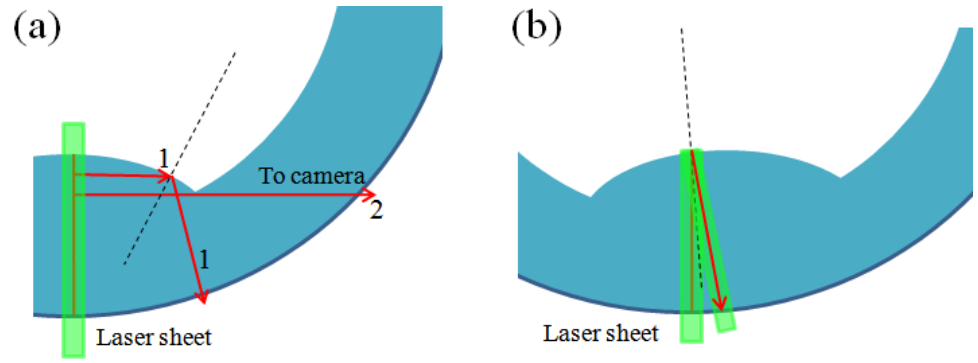



**Figure 13**: Schematic showing the effect of transverse film slope on the film-thickness measurement: (a) in PLIF90, and (b) in BBLIF.

In Fig. 13(a), only the image of the film between the wall and Ray 2 appear in the PLIF90 image, leading to an underestimation of film thickness; the region above Ray 2 will be hidden to the camera owing to either refraction (if the slope is very steep) or TIR (at lower slopes) at the liquid-gas interface. It should be noted that PLIF70 is expected to be less sensitive to this type of distortion than PLIF90, since the transverse slope of the interface will rarely attain large enough angles to hide the true interface, and thus in the majority of cases, the entire illuminated section of the flow will be visible. Nonetheless, on top of disturbance waves, fast ripples and especially liquid bags/ligaments may display higher transverse slopes, which may also affect the PLIF70 measurement at these locations.

In Fig. 13(b), the transverse slope leads to an increased incidence angle at the interface, which was previously associated with an overestimation of film thickness by BBLIF, and off-axis reflections that excite a different fluid volume, not in accordance with Eq. (1) which is subject to the assumption that the original and reflected excitation light rays are collinear and overlapping through the same fluid volume. These effects are expected to lead to local overestimations of film thickness due to the reflected light, which can be significant, as well as spatial averaging and reduced spatial resolution. The above hypotheses will be re-examined later on based on direct comparisons between film-thickness measurements generated by the two LIF approaches.

### 3.4. Detection of bubbles

The aeration of liquid films (i.e., presence of bubbles inside the films) is common in annular flows and would be expected to affect strongly the heat and mass transfer, shear stress/pressure drop, and (if relevant) chemical reaction rates in relevant multiphase systems, yet the relevant flow-regimes have not been investigated in great detail. Some noteworthy efforts include the study of Rodriguez and Shedd (2004) who used backlit imaging to obtain bubble-size distributions inside the substrate-film layer between disturbance waves, and the study by Zadrazil et al. (2014) who used PLIF to measure both the size and frequency of the bubbles. Finally, Cherdantsev et al. (2017) investigated the bubbles generated during droplet-impact events onto a gas-sheared liquid film using 3-D BBLIF.

In this section, we present and analyze a sample PLIF and BBLIF image pair that contains bubbles (Fig. 14a), in order to assess the reliability of bubble detection by the two techniques, and to examine the effect that their presence has on the local film-thickness measurement. Based on visual inspection of the two frames, the majority of the bubbles that appear in the PLIF frame are not located within the excitation plane. For example, the bubbles marked (1) are located between the excitation plane and the PLIF camera, whilst the bubbles marked (2) are located behind the excitation plane; only the bubbles marked (3) are located inside the excited region of the flow. Additional bubble images can be detected in the PLIF frame above the gas-liquid interface (red trace as identified by BBLIF). Provided that the latter is indeed the true interface in

this smooth interface region, these bubble images appear due to the mirror effect. Therefore, raw counting of bubbles on PLIF images will lead to an overestimate.

Despite this deficit, PLIF can still be used to conduct bubble-frequency measurements, provided that a thorough analysis of the brightness distribution within each bubble is performed. In particular, we observe that any bubbles located inside the excitation plane cause a pronounced reduction in the local fluorescence intensity, while any bubbles located behind the excitation plane mainly become visible because they reflect the fluorescence emitted by the illuminated liquid volume (see, e.g., Fig. 14b, Bubble 2). The brightness at the centres of the images of such bubbles is of roughly the same brightness as the rest of the fluorescing film-region, however, the edges of the bubbles glow brighter as they reflect light from large portions of the fluorescing liquid-volume. Any bubbles that are located between the laser sheet and the camera become visible due to both the passing and reflected fluorescent light (see, e.g., Fig. 14(b), Bubble 1). The reflected light is mostly visible along the edges of the bubbles in the axial direction of the flow, while the passing light creates an ellipsoid-shaped bright spot bound by darker regions at the upper and lower borders of the bubbles. These regions appear due to TIR of the transmitted light (see, e.g., Ray *a* in Fig. 14(c)). Alternatively, two or more PLIF cameras, on either side of the illumination plane or otherwise, can be used to identify common bubbles.

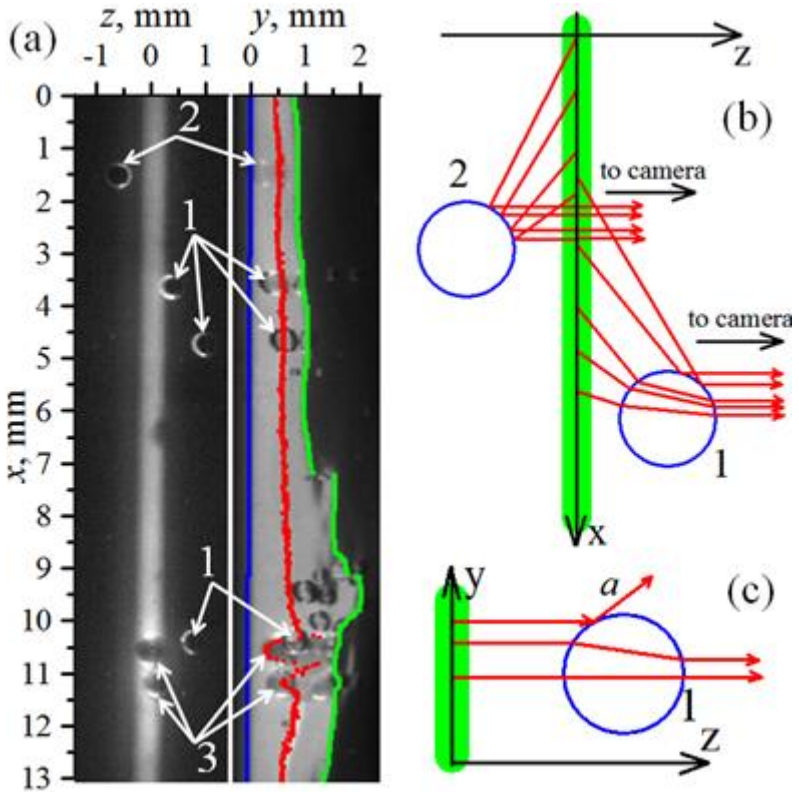



**Figure 14**: (a) Raw PLIF70 and BBLIF images of a film region containing bubbles from a flow with $Re_L$ = 300 and $Re_G$ = 43,700. The numbers represent bubbles located: (1) in front of the laser sheet, (2) behind the laser sheet, and (3) inside the laser sheet. (b, c) Ray tracing illustrations for the first two situations. The coloured lines in (a) are explained in Fig. 8.

In the BBLIF images, bubbles appear as thin, bright rings (see, e.g., the left frame of Fig. 14a). The centres of the bubbles are darker than the surrounding film as the bubbles do not contain any fluorescent marker, while the bright rims are attributed to TIR of the excitation light at the bubble edges. In the PLIF frame, the location of the BBLIF gas-liquid interface (shown as a red trace) can be directly compared to the location of the bubbles that are found inside the excitation plane (i.e., those marked (3)). The upper bubble is located in the middle of

the laser sheet (across the excitation plane) and thus, if we neglect the curvature of the various interfaces, the local BBLIF measurement, $h_{BB}$, corresponds to the 'residual' thickness of the film, that is, to the total thickness of two liquid-layers above and below the bubble. In the PLIF frame, the BBLIF measurement lies slightly above the bottom of the bubble, which is due to the thickness of the liquid layer above the bubble. The lower bubble is located at a slightly offset relative to the centre of the laser sheet (again across the excitation plane), and thus, the trough in the $h_{BB}$ measurement is smaller as a larger liquid volume is integrated. If only the border of the bubble was located inside the sheet, then the bubble would yield a local peak instead of a trough in the $h_{BB}$ measurement, in the same manner as the borders of the first bubble yield erroneously large $h_{BB}$ values at its upper and lower edges. Finally, as neither 2-D, nor 3-D BBLIF provide direct measurements of the thickness of the film surrounding the bubbles or the size of the bubbles in the $y$-direction, the only way to estimate these quantities is by interpolating the film thickness from outside the bubbles. PLIF, instead, can recover such measurements since the excited film-region is visualized directly, provided that the mirror effect is suppressed and there are no bubbles in the line-of-sight of the camera blocking the location of the true gas-interface. As above, two or more PLIF cameras, e.g., on either side of the illumination plane or otherwise, can be used to assist with identifying in- and out-of-plane bubbles.

### 3.5. Rough films

At the rough surface of disturbance waves we encounter all optical effects that were discussed in the previous sections as inducing errors in the film-thickness measurements. These effects include the overestimation of the film thickness by PLIF due to the mirror effect when the films are smooth and loss of signal in thin/near-wall film regions, the overestimation of the film thickness and loss of resolution or signal by BBLIF due to reflections when the film slopes are steep or when the films are thick, and the underestimation or loss of resolution of the film thickness by both techniques due to the 3-D shape of the waves. Additional effects include the presence of multiple bubbles and entrainment of liquid in the gas phase if this comes into contact or in proximity to the interface.

In the absence of bubbles, the steep slopes that affect the BBLIF measurement are mostly observed in the presence of fast ripples that ride the disturbance waves, as well as over the disturbance waves or other large-amplitude waves themselves. In the images presented by Cherdantsev et al. (2014), the entire horseshoe-shaped fronts of the fast ripples show non-physical high amplitudes; such slopes may be present not only along the centres of the fronts of fast, 3-D ripples but also at the edges of the horseshoe wave fronts, and result in the appearance of erroneous longitudinally-oriented peaks in the film-thickness. As the circumferential span of the fast ripples typically varies in the range 5 – 10 mm, the probability also exists of the side slope of a fast ripple being found between the excitation plane and the camera, resulting in the disappearance of the ripple from the PLIF images, especially in the case of PLIF90. Steep slopes are also found inside the liquid bags/ligaments that are generated during the impact of droplets onto the film surface, as well as in the periphery of bubbles trapped inside the film (which is a very frequent phenomenon, as evidenced by the frames presented in Fig. 15), also resulting in local overestimations by BBLIF.

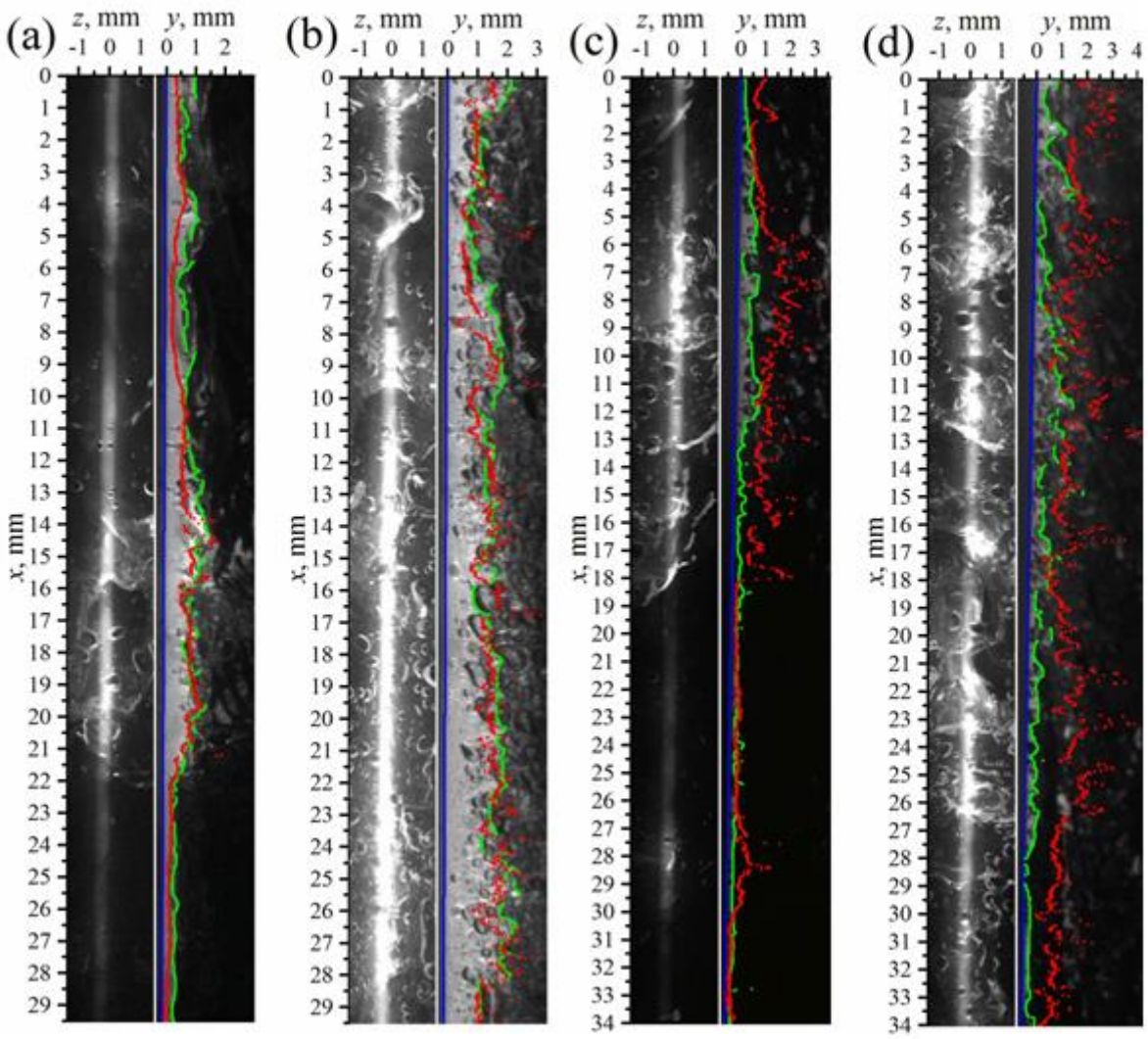



**Figure 15**: Example results showing the recovered location of the gas-liquid interface as identified by: (a, b) PLIF70 and BBLIF, and (c, d) PLIF90 and BBLIF, in flows with: (a, c) $Re_L$ = 300 and $Re_G$ = 78,600, and (b, d) $Re_L$ = 1,330 and $Re_G$ = 52,400.

In Fig. 15, we present some examples of film-thickness measurements recovered by PLIF90, PLIF70 and BBLIF under highly sheared (and thus highly agitated and aerated) annular-flow conditions that demonstrate the range of results that can be obtained by these techniques. In some cases, the agreement is acceptable and in others the PLIF and BBLIF data are not in good agreement. The BBLIF data contain many narrow peaks, which appear either due to local steep interface-slopes due to waves or due to bubbles entrained in the liquid. In the thin base film ahead of large waves, when a smooth-interface is encountered along the waves, PLIF typically overestimates the film thickness locally.

## 4. Quantitative comparisons

The theoretical framework developed in Section 2 and the frame-by-frame comparisons in Section 3 have provided us with a better understanding of the strengths and weaknesses of the two LIF techniques. We now proceed to direct quantitative comparisons of film-thickness data that were recovered simultaneously in our flows of interest by PLIF ($h_P$) and BBLIF ($h_{BB}$). Specifically, we compare mean film-thickness, film-thickness standard deviation and film roughness data in Section 4.1, and compile joint probability-density

distributions of film thickness in Section 4.2. Finally, we propose corrections to raw PLIF and BBLIF data depending on the wave regime and measurement configuration characteristics.

### 4.1. Statistical moments

In Fig. 16, we present film-thickness statistics recovered by the employment of PLIF90, PLIF70 and BBLIF over a range of liquid and gas flow-rates. Two gas velocities are selected for these comparisons: i) $Re_G = 0$ which relates to falling films, and ii) $Re_G = 52{,}400$ which triggers a significant increase in the film roughness. In Fig. 16(a), the mean film thicknesses, $\langle h \rangle$, which are calculated using the entire $h(x,t)$ datasets from each flow condition are plotted as a function of the flow $Re_L$. When $Re_G = 0$, $\langle h_{BB} \rangle$ matches the predictions by the Nusselt solution to the Navier-Stokes equation, especially below $Re_L \approx 500$. For these laminar flows with (largely) smooth interfaces, BBLIF can be considered a reliable measurement technique. Local errors due to the effects of steep or 3-D waves are less frequent in these flows and will not significantly affect this average measurement. Above this $Re_L$ value, both the BBLIF and PLIF data show a slight increase; a behaviour that has been observed by many researchers in the past and that has been attributed to the transition from laminar to turbulent flow (see, e.g., Mudawar and El-Masri, 1986). PLIF90 and PLIF70 display consistently higher $\langle h \rangle$ values in the same flow conditions, which is attributed to the mirror effect. Specifically, the mean film-thicknesses measured by PLIF90 are typically ≈ 30 % higher than those measured by BBLIF (see Fig. 16(a)), while in the case of PLIF70 the deviation is higher. As shown in Fig. 16(b), the ratio between the PLIF and BBLIF $\langle h \rangle$ data decreases with increasing $Re_L$ (and, hence, with increasing film thickness), in accordance with the prediction provided in Fig. 10(c). For films at higher $Re_L$, a general underprediction of the mean film-thickness is expected by BBLIF owing to the limitations associated with the maximum film-thickness measurement discussed in Section 2.3.

The imposition of a co-current gas shear results in a decrease in the average film-thickness measurements by all three methods. The mean film-thickness values by PLIF90 now lie both above (low $Re_L$) and below (high $Re_L$) those by BBLIF. PLIF70 still yields larger values than both PLIF90 and BBLIF, though both ratios between PLIF and BBLIF decrease with increasing $Re_L$, which suggests that the mirror effect is strongly suppressed by the three-dimensionality of the interface. Evidence to support this statement comes mainly from the PLIF90 results, which are now lower than BBLIF. In the BBLIF measurements, the frequent passage of bubbles is now most probably contributing to significant overestimations locally (at the edges of the bubbles) and underestimations locally over the bulk of the bubbles, which would impact the mean, but even more so the higher order statistics of the film-thickness measurement. At the highest $Re_L$, the ratio between PLIF90 and BBLIF drops well below unity, to 0.75 at $Re_L = 1{,}330$.

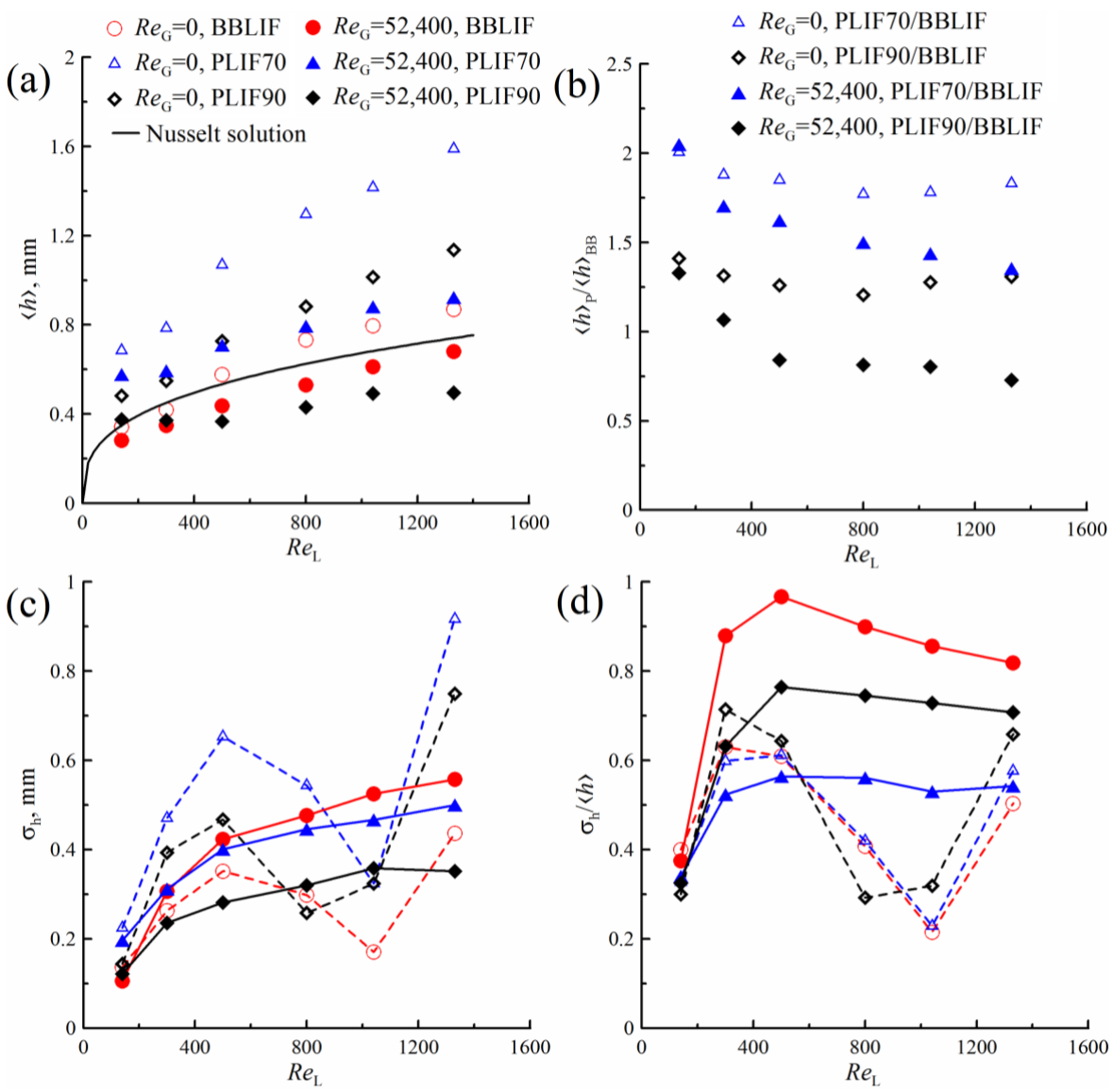



**Figure 16**: Film-thickness statistics obtained by the three LIF techniques (BBLIF, PLIF70 and PLIF90), for flows with $Re_G$ = 0 and $Re_G$ = 52,400, over the entire range of examined $Re_L$: (a) mean film-thicknesses data, (b) ratios of the mean film-thicknesses measured by different PLIF approaches to those measured by BBLIF, (c) film-thickness standard deviation data, and (d) film roughness data.

Alongside the mean film-thickness results, absolute film-thickness standard deviations, $\sigma_h$, and film roughness, $\sigma_h/\langle h\rangle$, results were also generated from the same datasets (see Fig. 16(c) and 16(d)) in order to examine how these statistical measures of the film waviness compare between the different techniques. When $Re_G$ = 0, the two PLIF techniques reveal the same overall trend for $\sigma_h$ as $Re_L$ is increased; a steep increase up to $Re_L \approx 500$, a drop at $Re_L \approx 800$, followed by a further rise. The $\sigma_h$ results obtained by BBLIF, in contrast, show a more gradual increase at progressively higher $Re_L$. The deviations between PLIF and BBLIF can be attributed mainly to the interface three-dimensionality.

In Fig. 16(d), we plot the (relative) film roughness, $\sigma_h/\langle h\rangle$, as a function of the flow $Re_L$ for the same range of flow conditions. In the falling films, we observe that the higher film roughness values we recover from all three techniques match relatively well. Although the absolute film thickness $\sigma_h$ measured by BBLIF increased gradually with $Re_L$, here $\sigma_h/\langle h\rangle$ experiences a maximum at intermediate $Re_L$ and a sharp rise at the highest $Re_L$, which is captured by all techniques. In rough films, the $\sigma_h$ measured by PLIF90, PLIF70 and BBLIF lie much closer, however, we expect that bubbles and other interfacial complexity is most probably

leading to the higher $\sigma_h/\langle h \rangle$ in the case of BBLIF. Consequently, the BBLIF data lie higher than the PLIF90 data, and are almost twice as high as the PLIF70 data for the same flow $Re_L$.

### 4.2. Probability density distributions

In this section, we present joint probability-density distributions, $P(h_P,h_{BB})$ with each $\{t,x\}$-combination in our film-thickness records contributing the $N^{th}$ measurement point in a 2-D bin, where the horizontal coordinate represents the $h_{BB}$ data and the vertical coordinate represents the $h_P$ data (Figs. 17 and 18). In Fig. 17, we examine the effect of the liquid and gas flow rates on distributions compiled using PLIF70 and BBLIF data from flows with $Re_L$ = 300 (left column) and $Re_L$ = 1,330 (right column), and $Re_G$ = 0 (top row column) and $Re_G$ = 52,400 (bottom row). The red lines represent $h_P = h_{BB}$, while the black lines show the predicted film-thickness for PLIF70 considering the overestimation due to the mirror effect as per Fig. 10. For the falling films (i.e., when $Re_G$ = 0), which are relatively smooth, the data follow the prediction based on Eq. (6) quite well, although we observe a larger scatter in the data at the higher liquid flow rates (and $Re_L$) and a deviation in thicker film regions. Thus, for most cases with $Re_G$ = 0 and low $Re_L$, the discrepancy between PLIF and BBLIF can mostly be described by the mirror effect. The excellent correspondence observed in the former case provides further evidence of the reliability of BBLIF when applied in smooth film flow regimes and regions.

Another interesting observation in Fig. 17(b) concerns the local deviations at higher film thicknesses for the flow cases with $Re_G$ = 0, and specifically the saturation-like behaviour when $h_{BB}$ > ~1.5 mm. As mentioned in Section 2.3, this behaviour is attributed to the narrow thickness of the laser-sheet and relative angle between the excitation laser-sheet plane and the optical axis of the BBLIF camera, which limit the maximum thickness that can be accurately measured by BBLIF setup, but also because the absorption that BBLIF relies upon is inherently nonlinear and saturates progressively for thicker films. In standalone BBLIF applications, these limitations can be reduced by careful selection of the dye concentration and laser intensity, and/or the employment of a narrower viewing angle and a thicker laser sheet, or 3-D BBLIF configuration as in Alekseenko et al. (2012) and Cherdantsev et al. (2014), however, this practice will lead to additional off-axes reflection errors at the complex 3-D interface whose influence on the total emission will be exacerbated, leading to significant local overestimations and/or smoothing and loss of spatial resolution.

Prior to the transition to the rough-film regime (i.e., in the range of $Re_G$ from 0 to ~30,000), the shapes of the distributions do not vary significantly with the flow $Re_L$. Beyond this transition, however, the distributions show more significant scatter. Though the majority of data points still tend to group around the black lines, at the higher liquid and gas flow rates (see, Fig. 17(d)), a significant fraction approaches the $h_{BB} = h_P$ line. In Sections 3.5 and 4, we noted that the rough surface of the disturbance waves suppresses the mirror effect, and that the presence of complex interfaces over or inside the liquid films results in local overestimations of the film-thickness by BBLIF. Increasing the gas velocity also results in a gradual shrinking of the range of observed film thicknesses for a fixed $Re_L$.

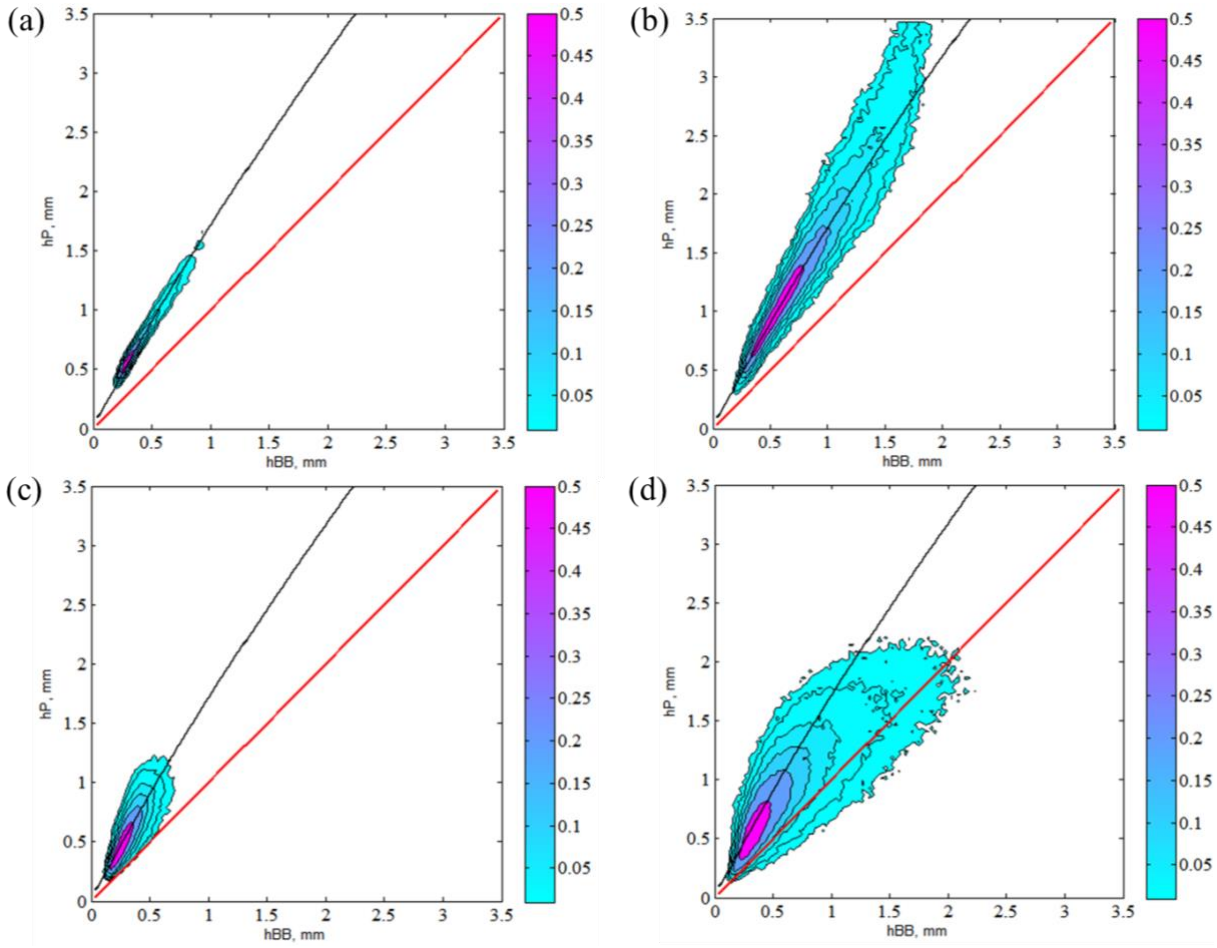



**Figure 17**: Joint-probability density distributions compiled using PLIF70 and BBLIF data for flows with $Re_L$ = 300 (left column), $Re_L$ = 1,330 (right column), $Re_G$ = 0 (top row) and $Re_G$ = 52,400 (bottom row). The colour scale indicates the joint probability, $P(h_P,h_{BB})$, with contours, encompassing, respectively, 50 %, 80 %, 90 %, 95 %, 98 % and 99 % of all data points. The red line corresponds to $h_P = h_{BB}$ and the black line shows the predicted film-thickness based on Eq. 6 and Fig. 10.

In Fig. 18, we revisit these results by employment of PLIF90 instead of the PLIF70 data. For the falling films, most data lie between the black and red lines, except at locally thick films (see Fig. 18(b)) where BBLIF shows a saturation-like behaviour similar that discussed in Fig. 17(b). These results suggest a weakening of the mirror effect and a stronger effect of the circumferential slopes of the film surface in the PLIF90 measurements compared to PLIF70 (see Section 3.3). With increasing gas flow rates, the data scatter increases and a significant fraction of PLIF90 data-points now lie below the $h_P = h_{BB}$ line. This finding is in line with the similar observation in Fig. 17 and suggests an overestimation of film-thickness by BBLIF in the presence of multiple and complex interfaces that are now encountered more frequently in these highly three-dimensional flows, as discussed earlier. As a result of these combined effects, the correspondence between PLIF90 and BBLIF is reduced compared to that between PLIF70 and BBLIF.

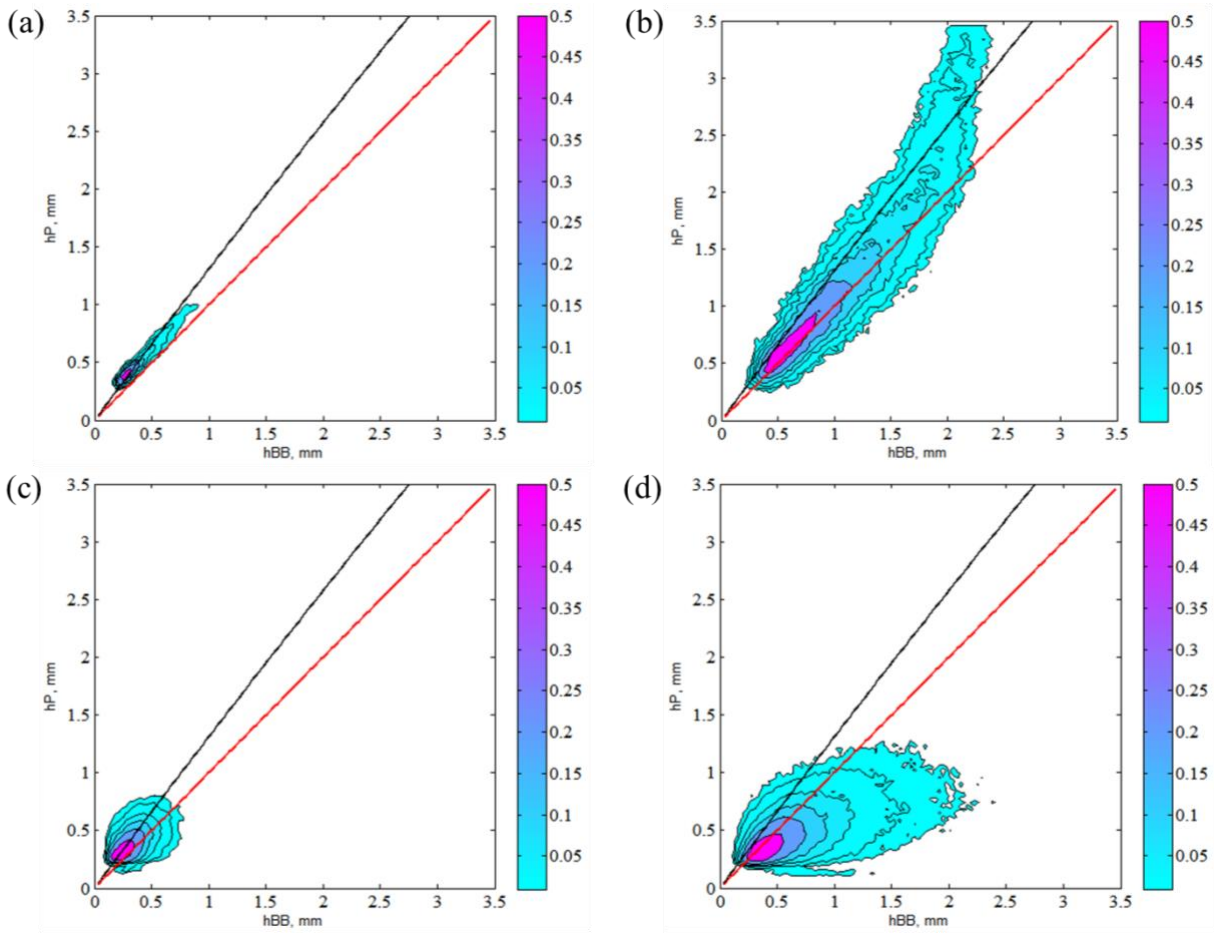



**Figure 18**: Joint-probability density distributions compiled using PLIF90 and BBLIF data for the same flows as in Fig. 17 with $Re_L$ = 300 (left column), $Re_L$ = 1,330 (right column), $Re_G$ = 0 (top row) and $Re_G$ = 52,400 (bottom row). For notation see Fig. 17. The red line corresponds to $h_P = h_{BB}$ and the black line shows the predicted film-thickness based on Eq. 4 and Fig. 10.

### 4.3. Correction procedures for standalone applications of PLIF and BBLIF

Amongst the two PLIF methods, PLIF70 has a lower dynamic range and sensitivity (for the same optical arrangement) than PLIF90 and is affected by the mirror effect to a larger extent, but is also less vulnerable to the three-dimensionality of the film which is increasingly important when requiring accurate spatiotemporally resolved information in flows with larger and more complex interfacial waves. Furthermore, in flows with smooth films regions for which BBLIF can be considered a reliable measurement technique, measurements by PLIF70 and BBLIF show a better agreement (higher correlation), whereas those by PLIF90 and BBLIF show a closer absolute numerical consistency but lower correlation in terms of trends, largely due to interfacial three-dimensionality which affects PLIF differently to BBLIF. Therefore, both PLIF techniques can be used subject an appreciation of their respective strengths, weaknesses and different errors, and specifically PLIF70 can be considered a reliable measurement in standalone applications especially in flows with complex interfaces, although it is necessary in this case to account for the stronger mirror effect it experiences in order to reduce the overall measurement error.

A correction procedure for PLIF70 is proposed here, which includes the recalculation of $h_P$ into a corrected film thickness using the analytical expressions provided in Section 3.2 for the smoother regions of the flow; when the interface is agitated, for example along the disturbance waves, $h_P$ should be taken as is. Unfortunately, it is difficult to identify the disturbance waves based on the local value of $h_P$ as the height of the base-film is often overestimated due to the mirror effect, causing a strong overlap between the $h_P$

corresponding to the base film and the waves. Instead, the disturbance waves can be identified based on their spatiotemporal behaviour, as was done by Alekseenko et al. (2014).

BBLIF can also be applied as a standalone technique, and when the film surface is smooth, does not require systematic corrections (although any random errors may be quite high; see Section 2.3). When large optical distortions ensue at the steep slopes of interfacial waves, however, it is difficult to recover the true interface shape due to the complex redistribution of the emitted light. On the other hand, these distortions can in some cases be identified and suppressed based on their shape, especially in simpler flows. Distortions with small longitudinal scale such as those encountered around isolated bubbles (see, for example, Fig. 14(a)) can be removed by application of median filtering to the obtained $h_{BB}(x)$ data. Larger distortions, such as those appearing at the fronts of the waves (see Figs. 12 and 15(a, b)), can again be identified from the slopes of the $h_{BB}(x)$ signals, and be partially accounted for. The procedure we propose comprises two main steps. Firstly, film regions with $dh_{BB}(x)/dx \geq 1$ are identified; this condition corresponds roughly to occurrence of TIR in the BBLIF measurements. For each such region, an area behind and an area ahead of it are identified using the criterion $dh_{BB}(x)/dx \leq -1$, which signifies the onset of the distorted region of the signal. The leftmost point of the first area, $x_1$, and the rightmost point of the second area, $x_2$, are marked as the borders of the distorted region, $x_2–x_1$, which is further processed if it extend by 50 pixels, or 1.34 mm, or less. These values are of course open to fine-tuning and a result of compromises based on the particulars of the BBLIF measurement implementation. Increasing this length further may result in overlapping of different distortion regions. Secondly, a parabolic approximation of the array $\{h_{BB}(x_1–1), h_{BB}(x_1), h_{BB}(x_2), h_{BB}(x_2+1)\}$ and respective $x$-coordinates are constructed between locations $x_1$ and $x_2$. If the sum of this approximation is less than the original sum of $h_{BB}(x_1{:}x_2)$, then the approximation is included in the film-thickness record in place of the original $h_{BB}$ values. It should be noted that we do not attempt to recover the true local film-thickness by employment of this procedure, but rather to discard any film-thickness values that are considered erroneous.

Examples of the application of the correction procedures described above, for both PLIF70 and BBLIF, are shown in Fig. 19 in the thin-film and large-wave regions of two flow regimes featuring disturbance waves. In particular, Fig. 19(a) and (c) show measurements recovered along the base film, with the corrected PLIF and BBLIF signals showing good agreement. The PLIF signals were corrected for the mirror effect, while the peaks around the bubbles were removed from the BBLIF signals. It can be seen from these figures that the proposed corrections introduce changes to the film thickness characteristics, which vary strongly with the local film thickness and interface structure, as well as other flow features such as bubbles inside the liquid film; nevertheless, the profiles in Fig. 19 reveal qualitatively the improvement in the match between the two techniques after the corrections are applied in these selected cases.

Furthermore, and arguably more importantly given the role of disturbance waves in these flows, Fig. 19(b) and (d) show measurements of highly agitated and aerated disturbance wave regions, where the roughness of the film suppresses the mirror effect, and which also boosts the apparent film-thickness measurement by BBLIF. Interestingly, the two techniques do not show good agreement along the presented wave topologies, which highlights the inherent difficulties in conducting space- and time-resolved measurements in such flow conditions by employment of optical diagnostic techniques and suggests that further work is necessary to overcome various and diverse error mechanisms.

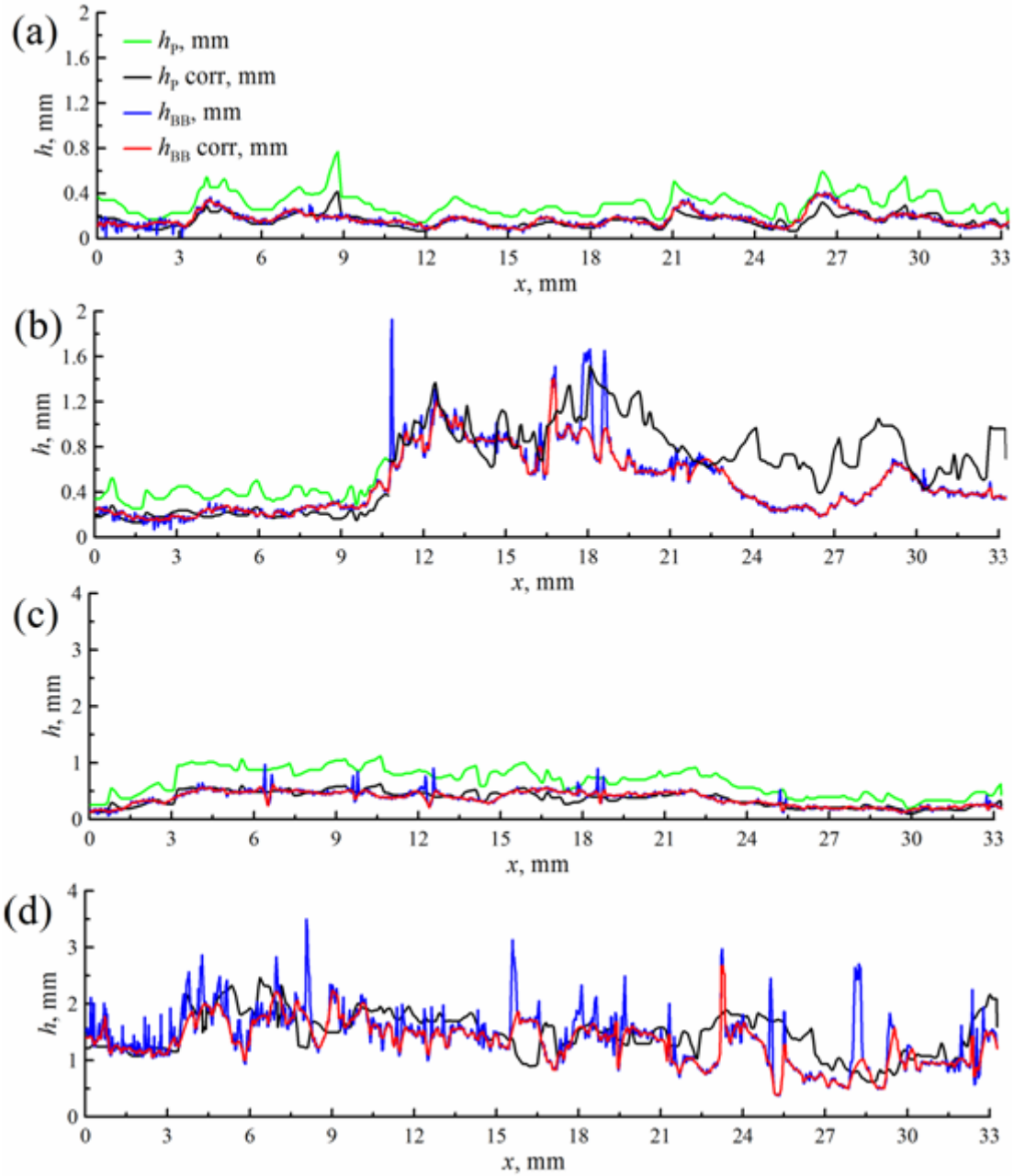



**Figure 19**: Correction procedure applied to PLIF70 and BBLIF data for flows with (a), (b) $Re_L$ = 300 and $Re_G$ = 78,600, and (c), (d) $Re_L$ = 1,330 and $Re_G$ = 52,400. The examples presented here relate to the base film (a, c) and the disturbance waves (b, d).

## 5. Conclusions

A detailed experimental investigation was performed involving the simultaneous application of two advanced optical methods for spatiotemporally resolved film thickness measurements, namely Planar Laser-Induced Fluorescence (PLIF) and Brightness-Based Laser-Induced Fluorescence (BBLIF), to co-current downward annular gas-liquid flows. Both techniques employ the principle of laser-induced fluorescence, but different methods for the film thickness calculation are used, making the techniques independent of each other. In the present set of experiments, the two techniques were deployed simultaneously using the same laser sheet as the excitation source, which also made it possible to perform direct comparisons of the two methods. The effect of the PLIF angle in the implementation of this technique was also considered. Specifically, in addition to the standard configuration in which the PLIF camera axis is positioned normal to the laser sheet plane

(referred to as PLIF90), a second configuration with the camera axis at an angle of 70° relative to the laser sheet (PLIF70) was also employed. New algorithms for PLIF image post processing are proposed, along with new approaches to obtain the required reference signal for BBLIF in the case of hydrophobic pipe materials.

Häber et al. (2015) predicted theoretically using ray-tracing analysis that the 'mirror effect', caused by total internal reflection of the fluorescent light at the gas-liquid interface, can lead to the appearance of a false image of the liquid film above the true interface and an overestimation of the film thickness by PLIF90. In the present work, the existence of this effect was confirmed experimentally for both PLIF90 and PLIF70 in the case of smooth and flat film regions, i.e., at low liquid and gas flow rates. Interestingly, bright or dark lines were occasionally observed inside raw PLIF images. As a general rule, the position of such lines agreed well with film thickness measurements by BBLIF, which suggests that these correspond to and indicate the real position of the interface. The overestimation of the film thickness due to the mirror effect by both PLIF90 and PLIF70 was evaluated in waveless films and showed good agreement with the experimentally measured ratio of film thickness measured by PLIF to that measured by BBLIF for a smooth and flat interface. At higher flow rates, especially of the gas, the interface became generally less smooth interface and it was found that in rougher wave regions, e.g., over disturbance waves, the mirror effect was much weaker, and eventually disappeared, due to scattering at the interface. In order to improve the PLIF method for standalone applications, a correction procedure was proposed (in Section 4.3) based on compensation for the mirror effect in smooth film regions and keeping the measured values otherwise.

BBLIF was found to be a reliable measurement method of film thickness in smooth and flat film regions (at free-surface angles up to ~40 – 45 ° to the horizontal), but can be affected by a loss of signal sensitivity and saturation in thick film regions, and is vulnerable to reflections of light through complex or multiple interfaces in agitated and/or aerated flow regions with significant wave activity that would appear with increasingly frequency at higher flow rates. It was also observed that BBLIF can lead to significant local overestimations of the film thickness in regions with higher interfacial slopes and/or curvature, e.g., at the fronts of the fast ripples, around bubbles and over disturbance waves, or localized underestimation in regions with multiple interfaces, which become progressively worse as the angle of total internal reflection is approached or exceeded. Such distortions may be reduced using the procedures suggested in Section 4.3. Issues relating to the dynamic range of the BBLIF measurement, its reduced measurement sensitivity and possible signal saturation especially when measuring thicker films in flows with large variations in film thickness need to be considered carefully in the experiment design stage, i.e., in selecting compromises between the BBLIF camera angle, dye concentration, exposure and other camera settings.

Both PLIF and BBLIF are also vulnerable to errors introduced by interfacial wave three-dimensionality, and in particular azimuthal/circumferential non-uniformity, which in the case of PLIF may lead to local film thickness underestimation and in the case of BBLIF to overestimation and reduced spatial resolution. Smaller angles between the laser sheet and the camera axis make the PLIF measurement less susceptible to this error.

Despite the much improved understanding of the strengths and limitations of the two LIF methods, non-trivial challenges remain in further reducing measurement errors and recovering more reliable and accurate information on the shape of more complex interfacial flows and phenomena, such as disturbance waves. These waves contain all the aforementioned possible sources of error, such as thick film regions and waves with significant three-dimensionality, steep slopes, high curvature, multiple scales and speeds, and highly agitated interfaces with multiple bubbles and droplets, which will affect any optical technique. The accurate measurement of disturbance waves remains a significant challenge for experimentalists, and new advances in this area, based on either LIF principle or (strongly recommended) hybrid combined methods, are required.

## Acknowledgements

The authors would like to thank Dr Ivan Zadrazil who was instrumental in supporting the implementation of these experiments, and the fruitful discussions concerning the processing of the resulting data. This work was supported by the Royal Society and UK Department for International Development (DFID), and by the UK Engineering and Physical Sciences Research Council (EPSRC) [grant numbers EP/K008595/1 and EP/L020564/1]. Data supporting this publication can be obtained on request from cep-lab@imperial.ac.uk.

## References

Adomeit, P., Renz, U., 2000. Hydrodynamics of three-dimensional waves in laminar falling films. Int. J. Multiph. Flow 26, 1183–1208.

Alekseenko, S.V., Antipin, V.A., Guzanov, V.V., Kharlamov, S.M., Markovich, D.M., 2005. Three-dimensional solitary waves on falling liquid film at low Reynolds numbers. Phys. Fluids 17(12), 121704.

Alekseenko, S.V., Antipin, V.A., Cherdantsev, A.V., Kharlamov, S.M., Markovich, D.M., 2009. Two-wave structure of liquid film and waves interrelation in annular gas-liquid flow with and without entrainment. Phys. Fluids 21(6), 061701.

Alekseenko, S., Cherdantsev, A., Cherdantsev, M., Isaenkov, S., Kharlamov, S., Markovich, D., 2012. Application of a high-speed laser-induced fluorescence technique for studying three-dimensional structure of annular gas-liquid flows. Exp. Fluids 53(1), 77–89.

Alekseenko, S.V., Cherdantsev, A.V., Heinz, O.M., Kharlamov, S.M., Markovich, D.M., 2013.Analysis of spatial and temporal spectra of liquid film surface in annular gas–liquid flow. Exp. Fluids 54(9), 1590.

Alekseenko, S.V., Cherdantsev, A.V., Heinz, O.M., Kharlamov, S.M., Markovich, D.M., 2014. Analysis of spatial and temporal evolution of disturbance waves and ripples in annular gas-liquid flow. Int. J. Multiph. Flow 67, 122–134.

Alekseenko, S.V., Aktershev, S.P., Bobylev, A.V., Kharlamov, S.M., Markovich, D.M., 2015a. Nonlinear forced waves in a vertical rivulet flow. J. Fluid Mech. 770, 350–373.

Alekseenko, S.V., Cherdantsev, A.V., Cherdantsev, M.V., Isaenkov, S.V., Markovich, D.M., 2015b. Study of formation and development of disturbance waves in annular gas–liquid flow. Int. J. Multiph. Flow 77, 65–75.

Azzopardi, B.J., 1983.Mechanisms of entrainment in annular two-phase flow. UKAEA Report AERE-R 11068, Harwell, UK.

Azzopardi, B.J., 1986. Disturbance waves frequencies, velocities and spacing in vertical annular two-phase flow. Nucl. Eng. Des. 92, 121–133.

Barbosa, J.R. Jr., Hewitt, G.F., Richardson, S.M., 2003. High-speed visualisation of nucleate boiling in vertical annular flow. Int. J. Heat Mass Transf. 46(26), 5153–5160.

Belt, R.J., Van't Westende, J.M.C., Prasser, H.M., Portela, L.M., 2010. Time and spatially resolved measurements of interfacial waves in vertical annular flow. Int. J. Multiph. Flow 36(7), 570–587.

Bonn, D., Rodts, S., Groenink, M., Rafai, S., Shahidzadeh-Bonn, N., Coussot, P., 2008. Some applications of magnetic resonance imaging in fluid mechanics: Complex flows and complex Fluids. Ann. Rev. Fluid Mech. 40, 209–233.

Charogiannis, A., An, J.S., Markides, C.N., 2015.A simultaneous planar laser-induced fluorescence, particle image velocimetry and particle tracking velocimetry technique for the investigation of thin liquid-film flows. Exp. Therm. Fluid Sci. 68, 516–536.

Charogiannis, A., Denner, F., van Wachem, B.G.M., Kalliadasis, S., Markides, C.N., 2017. Detailed hydrodynamic characterization of harmonically excited falling-film flows: A combined experimental and computational study. Phys. Rev. Fluids 2(1),014002.

Chen, Z.Q., Hermanson, J.C., Shear, M.A., Pedersen, P.C., 2005. Ultrasonic monitoring of interfacial motion of condensing and non-condensing liquid films. Flow Meas. Instrum. 16(6), 353–364.

Cherdantsev, A.V., Hann, D.B., Azzopardi, B.J., 2014. Study of gas-sheared liquid film in horizontal rectangular duct using high-speed LIF technique: Three-dimensional wavy structure and its relation to liquid entrainment. Int. J. Multiph. Flow 67, 52–64.

Cherdantsev, A.V., Hann, D.B., Hewakandamby, B.N., Azzopardi, B.J., 2017. Study of the impacts of droplets deposited from the gas core onto a gas-sheared liquid film. Int. J. Multiph. Flow 88, 69–86.

Chu, K.J., Dukler, A.E., 1974. Statistical characteristics of thin, wavy films: Part II. Studies of the substrate and its wave structure. AIChE J. 20(4), 695–706.

Clark, W.W., Campbell, G.B., Hills, J.H., Azzopardi, B.J., 2001.Viscous effects on the interfacial structure of falling liquid film/co-current gas systems. Proc. 4th Int. Conf. Multiph. Flow, 2001, New Orleans, USA.

Damsohn, M., Prasser, H.M., 2009. High-speed liquid film sensor for two-phase flows with high spatial resolution based on electrical conductance. Flow Meas. Instrum. 20(1), 1–14.

Dupont, J., Mignot, G., Zboray, R., Prasser, H.M., 2016. Infrared film thickness measurement: Comparison with cold neutron imaging. J. Nucl. Sci. Technol. 53(5), 673-681

Farias, P.S.C., Martins, F.J.W.A., Sampaio, L.E.B., Serfaty, R., Azevedo, L.F.A., 2012. Liquid film characterization in horizontal, annular, two-phase, gas–liquid flow using time-resolved laser-induced fluorescence. Exp. Fluids 52(3), 633–645.

Fischer, F., Hampel, U., 2010. Ultra fast electron beam X-ray computed tomography for two-phase flow measurement. Nucl. Eng. Des. 240(9), 2254–2259.

Häber, T., Gebretsadik, M., Bockhorn, H., Zarzalis, N., 2015. The effect of total reflection in PLIF imaging of annular thin films. Int. J. Multiph. Flow 76, 64–72.

Han, H., Zhu, Z., Gabriel, K., 2006.A study on the effect of gas flow rate on the wave characteristics in two-phase gas–liquid annular flow. Nucl. Eng. Des. 236(24), 2580–2588.

Hazuku, T., Takamasa, T., Matsumoto, Y., 2008.Experimental study on axial development of liquid film in vertical upward annular two-phase flow. Int. J. Multiph. Flow 34(2), 111–127.

Hewitt, G.F., Hall Taylor, N.S., 1970.Annular two-phase flow. Pergamon Press, Oxford, UK.

Hewitt, G.F., Lovegrove, P.C., Nicholls, B., 1964. Film thickness measurement using a fluorescence technique I: Description of the method. UKAEA Report AERE-R4478, Harwell, UK.

Hewitt, G.F., Jayanti, S., Hope, C.B., 1990. Structure of thin liquid films in gas-liquid horizontal flow. Int. J. Multiph. Flow 16(6), 951–957.

Hurlburt, E.T., Newell, T.A., 1996. Optical Measurement of Liquid Film Thickness and Wave Velocity in Liquid Film Flows. Exp. Fluids 21(5), 357–362.

Karapantsios, T.D., Paras, S.V., Karabelas, A.J., 1989. Statistical characteristics of free falling films at high Reynolds numbers. Int. J. Multiph. Flow 15(1), 1–21.

Kharlamov, S.M., Guzanov, V.V., Bobylev, A.V., Alekseenko, S.V., Markovich, D.M., 2015. The transition from two-dimensional to three-dimensional waves in falling liquid films: Wave patterns and transverse redistribution of local flow rates. Phys. Fluids 27, 114106.

Kokomoor, W., Schubring, D., 2014. Improved visualization algorithms for vertical annular flow. J. Vis. 17(1), 77–86.

Lel, V.V., Al-Sibai, F., Leefken, A., Renz, U., 2005. Local thickness and wave velocity measurement of wavy films with a chromatic confocal imaging method and a fluorescence intensity technique. Exp. Fluids 39(5), 856–864.

Liu, J., Paul, J.D., Gollub, J.P., 1993. Measurements of the primary instabilities of film flows. J. Fluid Mech. 250, 69–101.

Markides, C.N., Mathie, R., Charogiannis, A., 2016. An experimental characterization of spatiotemporally resolved heat transfer in thin liquid-film flows falling over an inclined heated foil. Int. J. Heat Mass Transf. 93, 872–888.

Mudawar, I.A., El-Masri, M.A., 1986. Momentum and heat transfer across freely falling turbulent liquid films. Int. J. Multiph. Flow 12(5), 771–790.

Nusselt, W., 1916. Die Oberflachenkondensation des Wasserdampfes.VDI Zeit. 60, 541–546.

Ohba, K., Nagae, K., 1993.Characteristics and behavior of the interfacial wave on the liquid film in a vertically upward air-water two-phase annular flow. Nucl. Eng. Des. 141(1-2), 17–25.

Pan, L.M., He, H., Ju, P., Hibiki, T., Ishii, M., 2015. Experimental study and modeling of disturbance wave height of vertical annular flow. Int. J. Heat Mass Transf. 89, 165–175.

Pham, S.H., Kawara, Z., Yokomine, T., Kunugi, T., 2014. Detailed observations of wavy interface behaviors of annular two-phase flow on rod bundle geometry. Int. J. Multiph. Flow 59, 135–144.

Schubring, D., Ashwood, A.C., Shedd, T.A., Hurlburt, E.T., 2010. Planar laser-induced fluorescence (PLIF) measurements of liquid film thickness in annular flow. Part I: Methods and data. Int. J. Multiph. Flow 36(10), 815–824.

Schubring, D., Shedd, T.A., 2011. A model for pressure loss, film thickness, and entrained fraction for gas–liquid annular flow. Int. J. Heat Fluid Flow 32(3), 730–739.

Sekoguchi, K., Takeishi, M., Ishimatsu, T., 1985. Interfacial structure in vertical upward annular flow. Physicochem. Hydrodyn. 6, 239–255.

Setyawan, A., Indarto, Deendarlianto, 2016. The effect of the fluid properties on the wave velocity and wave frequency of gas-liquid annular two-phase flow in a horizontal pipe. Exp. Therm. Fluid Sci. 71, 25-41.

Sharaf, S., Da Silva, M., Hampel, U., Zippe, C., Beyer, M., Azzopardi, B., 2011. Comparison between wire mesh sensor and gamma densitometry void measurements in two-phase flows. Meas. Sci. Technol. 22, 104019.

Takenaka, N., Asano, H., Fujii, T., Matsubayashi, M., 1998. Three-dimensional visualization of void fraction distribution in steady two-phase flow by thermal neutron radiography. Nucl. Eng. Des. 184(2-3), 203–212.

Van der Meulen, G.P., 2012. Churn-annular gas-liquid flows in large diameter vertical pipes. Ph.D. Thesis, University of Nottingham, UK.

Vlachogiannis, M., Bontozoglou, V., 2001. Observations of solitary wave dynamics of film flows. J. Fluid Mech. 435, 191–215.

Webb, D., Hewitt, G.F., 1975. Downwards co-current annular flow. Int. J. Multiph. Flow 2(1), 35–49.

Woodmansee, D.E., Hanratty, T.J., 1969. Mechanism for the removal of droplets from a liquid surface by a parallel air flow. Chem. Eng. Sci. 24(2), 299–307.

Zadrazil, I., Matar, O.K., Markides, C.N., 2014. An experimental characterization of downwards gas–liquid annular flow by laser-induced fluorescence: Flow regimes and film statistics. Int. J. Multiph. Flow 60, 87–102.

Zadrazil, I., Markides, C.N., 2014. An experimental characterization of liquid films in downwards co-current gas–liquid annular flow by particle image and tracking velocimetry. Int. J. Multiph. Flow 67, 42–53.

Zhao, Y., Markides, C.N., Matar, O.K., Hewitt, G.F., 2013. Disturbance wave development in two-phase gas–liquid upwards vertical annular flow. Int. J. Multiph. Flow 55, 111–129.